Data assimilation and linear analysis with turbulence modelling: Application to airfoil stall flows with PIV measurements

Vincent Mons, Arthur Vervynck, Olivier Marquet

Noname manuscript No.
(will be inserted by the editor)

Data assimilation and linear analysis with turbulence modelling: Application to airfoil stall flows with PIV measurements

Vincent Mons · Arthur Vervynck · Olivier Marquet

Abstract A combined data-assimilation and linear mean-flow analysis approach is developed to estimate coherent flow fluctuations from limited mean-flow measurements. It also involves Reynolds-Averaged Navier-Stokes (RANS) modelling to efficiently tackle turbulent flows. Considering time-averaged Particle Velocimetry Image (PIV) measurements of the near-stall flow past a NACA0012 airfoil at an angle of attack of 10° and in the chord-based Reynolds number range $4.3 \cdot 10^4 \leq Re \leq 6.4 \cdot 10^4$, data assimilation is first employed to correct RANS equations that are closed by the Spalart-Allmaras model. The outputs of this procedure are a full mean-flow description that matches the PIV data and a consistent turbulence model that provides not only a mean eddy-viscosity field but also the perturbations of the latter with respect to mean-flow modifications. Global stability and resolvent analyses are then performed based on the so-obtained mean flow and model to satisfactorily predict near-stall low-frequency phenomena, as confirmed through comparison with the Spectral Proper Orthogonal Decomposition (SPOD) of the PIV measurements. This comparison also allows to highlight the benefits in taking into account variations in the turbulent eddy-viscosity over a frozen approach for the correct estimation of the present coherent low-frequency oscillations.

1 Introduction

The understanding and modelling of the airfoil stall regime remains an active research area and is of paramount importance in the design of aeronautical systems. Stall corresponds to significant flow separation and a drop in lift, and thus in the aerodynamic performances, for angles of attack that are higher than a critical value that depends on the flow's and airfoil's characteristics [31]. Stall may also be associated to other complex flow phenomena such as hysteresis [56], the emergence of steady three-dimensional patterns [70] or the occurrence of low-frequency oscillations [73], in particular at relatively low chord-based Reynolds numbers that

Vincent Mons E-mail: vincent.mons@onera.fr · Arthur Vervynck · Olivier Marquet
DAAA, ONERA, Institut Polytechnique de Paris, 92190, Meudon, France

verify $10^4 \lesssim Re \lesssim 3 \cdot 10^5$, which correspond to typical values for unmanned aerial vehicles and low-pressure turbines, among other applications.

In this context, and as further elaborated below, the aim of the present study is to contribute to the development of affordable numerical approaches for the accurate prediction of airfoil stall and related phenomena. This will be here achieved through a two-step procedure, which will first consist in inferring a mean-flow description and associated model from experimental results. In a second step, linear analyses will be employed to estimate dynamical flow features.

In the range $10^4 \lesssim Re \lesssim 3 \cdot 10^5$, the flow may exhibit separation of the laminar boundary layer at the suction side of the airfoil close to the leading edge, which then experiences transition to turbulence, possibly followed by its reattachment further downstream on the suction side, therefore forming a so-called laminar-separation bubble [65]. This latter flow structure appears to play a key role in stall and in the appearance of some of the above-mentioned phenomena, in particular that of low-frequency flow oscillations, which will be particularly investigated in the present study. Such low-frequency phenomena were first identified experimentally [73, 8, 49, 64] and then further investigated numerically [53, 50, 1, 15]. They occur at frequencies that are at least one order of magnitude lower than those associated to vortex-shedding phenomena and correspond to large-scale velocity fluctuations over the whole suction side that are essentially two-dimensional, making the flow alternate between more attached states and detached ones, which are associated to higher and lower lifts, respectively.

The above-mentioned characteristics of such oscillations and the turbulent nature of the present flows of interest make the latter difficult to fully and accurately capture through experiments or high-fidelity simulations. On the one hand, they involve small-scale and high-frequency phenomena such as laminar separation at the leading edge of the airfoil and the development of Kelvin-Helmholtz instabilities in the separated shear layer, requiring high spatio-temporal resolution to depict. On the other hand, the presence of low-frequency and large-scale oscillations in the flow imposes sufficiently large field of view and acquisition/simulation time to be correctly captured. Such considerations motivate the development of alternative approaches to investigate the physics of near-stall airfoil flows. In this study, we will rely on a reduced-order modelling approach that is based on a linear framework, namely resolvent analysis.

Resolvent analysis [32, 6], which may also be referred to as input-output analysis in the literature, relies on the linearization of governing equations around a time-averaged mean flow. In this framework, omitted nonlinearities are treated as a harmonic forcing to such linear equations, which form the so-called resolvent operator, and flow fluctuations at a given frequency are estimated through the identification of the most amplified forcing distributions by the resolvent operator. Application of resolvent analysis to the characterization of fluctuations in airfoil flows, focusing on vortex-shedding and/or Kelvin-Helmholtz phenomena, may be found in [66, 67, 72, 63, 71, 29], among others.

It is first worth mentioning that all the mentioned studies relied on the laminar Navier-Stokes equations to build the resolvent operator, i.e. performed the linearization of the momentum equations around the investigated mean flows while considering only a kinematic viscosity (referred to as ν-model in [39]). However, an increasing body of literature on wall-bounded [39, 62] and jet flows [47, 25] clearly supports the use of eddy-viscosity models in resolvent analysis for a better identi-

fication of coherent fluctuations, which are considered distinct from turbulent ones according to a triple decomposition of the flow [23]. Beyond the utility of turbulence modelling, a more open question concerns the necessity or not to take into account perturbations in the turbulent eddy-viscosity with respect to mean-flow modifications when linearizing the mean-flow governing equations to derive the resolvent operator. In the vast majority of resolvent analysis studies, with very few exceptions [54, 52], such perturbations in the turbulent eddy-viscosity are omitted, which is referred to as the frozen eddy-viscosity approach in the following, while they were taken into account in a number of global stability analyses as performed in [13, 33, 54, 10], which will be referred to as the perturbed eddy-viscosity approach in the following. In these latter studies, the perturbations in the turbulent eddy-viscosity were evaluated through the one-equation Spalart-Allmaras model [59], which is particularly appropriate for aerodynamic applications.

Aside from modelling aspects, another key ingredient in resolvent analysis is the mean flow around which the analysis is performed. In most above-mentioned studies, such a mean flow is obtained from either high-fidelity simulations or well-resolved experiments, which, as detailed above, are challenging to perform for near-stall airfoil flows. An alternative approach may consist in relying on Reynolds-Averaged Navier-Stokes (RANS) simulations to get the required mean flow, as in the above-mentioned stability analysis studies. However, near-stall flows are known to be challenging for RANS models, in particular in the considered transitional regime ($10^4 \lesssim Re \lesssim 3 \cdot 10^5$). A more original strategy may rely on limited data, as provided by experiments, and employ data assimilation techniques [28, 21] to infer a full mean-flow description from the latter. This was notably performed in the context of resolvent analysis in [63], where Particle Image Velocimetry (PIV) measurements of the flow around a NACA0018 airfoil at $Re \simeq 10^4$ were assimilated in conjunction with the steady laminar Navier-Stokes equations through the optimization of a forcing term in the momentum equations that accounts for the full Reynolds stress tensor, following [16, 61].

Compared to this latter work, we here propose to rely on turbulence modelling, still employing data assimilation to allow the consideration of limited mean-flow measurements as a basis for linear mean-flow analyses. The use of RANS models greatly facilitates the numerical handling of higher Reynolds flows compared to the use of the steady laminar Navier-Stokes equations, and, as mentioned above, enables the introduction of a distinction between coherent and turbulent fluctuations in mean-flow analyses. In the present study, we consider as configuration the near-stall flow past a NACA0012 airfoil at an angle of attack of 10° in the Reynolds number range $4.3 \cdot 10^4 \leq Re \leq 6.4 \cdot 10^4$. Time-averaged PIV measurements, which do not provide alone a full description of the mean-velocity field, are available for this configuration. As a first step, full mean flows are obtained from these measurements based on a data assimilation procedure that consists in correcting the RANS equations closed by the Spalart-Allmaras model. The latter model, in its baseline form, does not allow to correctly capture the present near-stall flows. The turbulence-modelling correction is determined so that the output of the RANS computations matches the PIV data in a least-square sense, similarly as in [57, 17, 5, 11]. This naturally provides a turbulent eddy-viscosity field that is consistent with the solved mean flow, following the terminology in [47, 52]. In a second step, the so-obtained mean flow and calibrated RANS model are employed in a resolvent analysis for the identification of coherent fluctuations, where

perturbations in the turbulent eddy-viscosity may be taken into account through the data-assimilation corrected Spalart-Allmaras model. The present approach is validated through comparison of the resolvent analysis results with the Spectral Proper Orthogonal Decomposition (SPOD) [68] of the PIV measurements, which allows to assess the benefits of the perturbed eddy-viscosity approach over the frozen one, focusing on the correct estimation of near-stall low-frequency phenomena.

The paper is organized as follows. §2 introduces the present framework of data assimilation and resolvent analysis for the estimation of coherent fluctuations. The flow configuration, PIV measurements and numerical methods are then described in §3. Data assimilation and linear mean-flow analyses results are discussed in §4. Finally, conclusions and perspectives are drawn in §5.

2 Data-consistent modelling and linear mean-flow analyses

2.1 Triple decomposition and closed equations for the coherent flow

We consider unsteady incompressible Newtonian flows. Following [23], flow variables such as the non-dimensional velocity field $\boldsymbol{u}$ are decomposed according to the following triple decomposition

$$\boldsymbol{u}(\boldsymbol{x},t) = \langle \boldsymbol{u} \rangle (\boldsymbol{x},t) + \boldsymbol{u}''(\boldsymbol{x},t), \quad \langle \boldsymbol{u} \rangle (\boldsymbol{x},t) = \bar{\boldsymbol{u}}(\boldsymbol{x}) + \boldsymbol{u}'(\boldsymbol{x},t), \tag{1}$$

where $< \circ >$ refers to a phase- or an ensemble-average that allows to extract the coherent part of the flow, while $\circ''$ denotes the remaining incoherent, turbulent part. The coherent component may be further decomposed as the sum of a steady contribution, which corresponds to the time-average of the flow, denoted by $\bar{\circ}$, and a purely fluctuating part $\circ'$. The exact non-dimensional governing equations for the coherent part of the flow are

$$\frac{\partial \langle \boldsymbol{u} \rangle}{\partial t} + \nabla \cdot \left(\langle \boldsymbol{u} \rangle \otimes \langle \boldsymbol{u} \rangle + \left\langle \boldsymbol{u}'' \otimes \boldsymbol{u}'' \right\rangle \right) + \nabla \langle p \rangle - Re^{-1} \Delta \langle \boldsymbol{u} \rangle = \boldsymbol{0}, \quad \nabla \cdot \langle \boldsymbol{u} \rangle = 0, \tag{2}$$

where p refers to the pressure field, while the definition of the Reynolds number Re for the present near-stall airfoil flows will be given in §3.1. The Reynolds-stress term $< \boldsymbol{u}'' \otimes \boldsymbol{u}'' >$ is closed based on the following Boussinesq approximation

$$\left\langle \boldsymbol{u}'' \otimes \boldsymbol{u}'' \right\rangle - \frac{2}{3} k \mathbf{I} = -2\nu_t \mathbf{S}(\langle \boldsymbol{u} \rangle), \tag{3}$$

where k and ν_t refer to turbulent kinetic energy and eddy-viscosity, respectively, while $\mathbf{S}(\circ) = \frac{1}{2}(\nabla \circ + (\nabla \circ)^{\mathrm{T}})$. The turbulent eddy-viscosity ν_t is here obtained through the Spalart-Allmaras model [59], which is generally considered as particularly appropriate for aerodynamic applications. This model provides a governing equation for a pseudo-eddy viscosity variable $\langle \tilde{\nu} \rangle$ from which is deduced ν_t through an algebraic relationship. This governing equation for $\langle \tilde{\nu} \rangle$ may be written as

$$\frac{\partial \langle \tilde{\nu} \rangle}{\partial t} + (\langle \boldsymbol{u} \rangle \cdot \nabla) \langle \tilde{\nu} \rangle - \nabla \cdot (\eta(\langle \tilde{\nu} \rangle) \nabla \langle \tilde{\nu} \rangle) - s(\langle \boldsymbol{u} \rangle, \langle \tilde{\nu} \rangle) = f_{\tilde{\nu}}(\langle \tilde{\nu} \rangle), \tag{4}$$

where η is a diffusion coefficient and $s = P_{\tilde{\nu}} + D_{\tilde{\nu}} + C_{\tilde{\nu}}$ is the sum of production, destruction and cross-diffusion terms [59]. In order to take into account finite-Reynolds number and transition effects in the considered flow configuration, the

modification in [60] and the algebraic transition model proposed in [41] are employed. The detailed expression of these terms is provided in appendix A. Equation (4) also involves a corrective field $f_{\tilde{\nu}}$, which has been here introduced to address the limitations of the Spalart-Allmaras model in correctly predicting the mean flows of interest, the baseline model corresponding to $f_{\tilde{\nu}} = 0$. The determination of this correction is the subject of §2.2. Equations (2)-(4) may be written in the following compact form

$$\mathbf{B}\frac{\partial \langle \boldsymbol{q} \rangle}{\partial t} + \boldsymbol{\mathcal{R}}(\langle \boldsymbol{q} \rangle) = \mathbf{0}, \quad \langle \boldsymbol{q} \rangle = \left(\langle \boldsymbol{u} \rangle^{\mathrm{T}}, \langle \Pi \rangle, \langle \tilde{\nu} \rangle \right)^{\mathrm{T}}, \quad \mathbf{B} = \begin{pmatrix} \mathbf{I} & 0 & 0 \\ 0 & 0 & 0 \\ 0 & 0 & 1 \end{pmatrix}, \tag{5}$$

where the modified pressure $\langle \Pi \rangle$ includes the contribution $\frac{2}{3}k$ and the non-linear operator $\boldsymbol{\mathcal{R}}$ is defined through

$$\boldsymbol{\mathcal{R}}(\langle \boldsymbol{q} \rangle) = \begin{pmatrix} \nabla \cdot \left(\langle \boldsymbol{u} \rangle \otimes \langle \boldsymbol{u} \rangle - 2(Re^{-1} + \nu_t(\langle \tilde{\nu} \rangle))\mathbf{S}(\langle \boldsymbol{u} \rangle) \right) + \nabla \langle \Pi \rangle \\ \nabla \cdot \langle \boldsymbol{u} \rangle \\ (\langle \boldsymbol{u} \rangle \cdot \nabla) \langle \tilde{\nu} \rangle - \nabla \cdot (\eta(\langle \tilde{\nu} \rangle) \nabla \langle \tilde{\nu} \rangle) - s(\langle \boldsymbol{u} \rangle, \langle \tilde{\nu} \rangle) - f_{\tilde{\nu}}(\langle \tilde{\nu} \rangle) \end{pmatrix}. \tag{6}$$

Instead of directly solving for (5) to determine the coherent flow $\langle \boldsymbol{q} \rangle = \bar{\boldsymbol{q}} + \boldsymbol{q}'$, we here rely on a more computationally tractable approach that consists in two main steps. First, the mean flow $\bar{\boldsymbol{q}}$ and consistent turbulent modelling are obtained through the data assimilation approach that is discussed in §2.2. In a second step, coherent fluctuations $\boldsymbol{q}'$ are estimated from linear analyses around the so-obtained mean flow, as detailed in §2.3.

2.2 Data-consistent mean flow and turbulence modelling

2.2.1 Mean-flow governing equations

As a first step of the above-mentioned procedure, we focus in this section on the determination of an appropriate mean flow $\bar{\boldsymbol{q}}$. The governing equations for the latter may be obtained through time-average of (5). Throughout this study, we rely on the hypothesis that coherent fluctuations $\boldsymbol{q}'$ are considered as small perturbations to the mean flow. Accordingly, contributions that originate from non-linear terms in the model operator $\boldsymbol{\mathcal{R}}$ and that involve products of coherent fluctuations (e.g. $\overline{\boldsymbol{u}' \otimes \boldsymbol{u}'}$) are considered as second- or higher-order contributions compared to other ones that depend on the mean flow only, and are therefore neglected. The mean flow should thus verify

$$\boldsymbol{\mathcal{R}}(\bar{\boldsymbol{q}}) = \mathbf{0}, \quad \bar{\boldsymbol{q}} = \left(\bar{\boldsymbol{u}}^{\mathrm{T}}, \bar{\Pi}, \bar{\tilde{\nu}} \right)^{\mathrm{T}}. \tag{7}$$

Equation (7) will be referred to as the Reynolds-Averaged Navier-Stokes (RANS) equations.

2.2.2 Variational data assimilation approach

As will be illustrated in the following, solving (7) with the baseline Spalart-Allmaras model does not provide accurate mean flows in the present near-stall configuration. This here motivates the use of variational data assimilation [26] to correct the latter turbulence model through the field $f_{\tilde{\nu}}$ that was introduced in (4), following [57,17,5,11]. Before proceeding further, a functional form is specified for $f_{\tilde{\nu}}$. While various proposals may be found in the latter-mentioned studies, the present choice was guided by the two following considerations. Firstly, as a turbulence-modelling correction, we want the latter to be restricted to turbulent regions and not to directly affect laminar ones that coexist in the present transitional flows. Secondly, as the identified correction will be then employed in the linear mean-flow analyses that are described in §2.3 to characterize coherent fluctuations, we want to avoid the model correction to be large in regions with high structural sensitivity [19] in order not to directly impact the output of such linear analyses and to easily get converged results. This led us to the following choice

$$f_{\tilde{\nu}}(\bar{\tilde{\nu}}) = g(\boldsymbol{x})\bar{\tilde{\nu}}^2, \tag{8}$$

where the multiplicative field $g(\boldsymbol{x})$ remains to be determined, and the factor $\bar{\tilde{\nu}}^2$ allows to address the two above considerations. This choice is further discussed in appendix B.

Considering time-averaged measurements $\bar{\boldsymbol{m}}$ of the flow of interest, the data assimilation problem is formulated as identifying the unknown field g in order to minimize the discrepancies between the computed mean flow $\bar{\boldsymbol{q}}$ and the measurements $\bar{\boldsymbol{m}}$. In a least-square framework, this leads to consider the following cost function J

$$J = J_m + J_p, \quad J_m = \frac{1}{2}\left\|\mathbf{H}\bar{\boldsymbol{q}} - \bar{\boldsymbol{m}}\right\|^2_{\mathcal{M}}, \tag{9}$$

where J_m quantifies the deviations between modelled and experimental quantities. The operator $\mathbf{H}$ allows to map the model space to the measurement one $\mathcal{M}$, whose associated scalar product is denoted by $\langle \circ, \circ \rangle_{\mathcal{M}}$. The corresponding definitions will be provided in §3.1 after having specified the nature of the present experimental data. The contribution J_p in (9) corresponds to a penalization term, whose role is to compensate for the limited character of the measurements and to ensure the well-posedness of the data assimilation problem. It is chosen as the squared $L^2(\Omega)$ norm of g, where Ω refers to the flow domain, namely

$$J_p = \frac{\beta}{2}\int_{\Omega} g^2 \, d\Omega, \tag{10}$$

where β is a weighting parameter to adjust the intensity of the penalization.

The minimization of the cost function J is performed through an iterative gradient-based descent approach. In order to take into account the equality constraint that is formed by the RANS equations in such an optimization procedure, we rely on the introduction of Lagrange multipliers, or adjoint state $\bar{\boldsymbol{q}}^\dagger$, which is solution of

$$\mathbf{L}^\dagger \bar{\boldsymbol{q}}^\dagger = \mathbf{H}^\dagger(\mathbf{H}\bar{\boldsymbol{q}} - \bar{\boldsymbol{m}}), \quad \bar{\boldsymbol{q}}^\dagger = \left(\bar{\boldsymbol{u}}^{\dagger\,\mathrm{T}}, \bar{\Pi}^\dagger, \bar{\tilde{\nu}}^\dagger\right)^{\mathrm{T}}, \tag{11}$$

where $\mathbf{H}^\dagger$ refers to the adjoint of the observation operator, while $\mathbf{L}^\dagger$ is the adjoint operator that is associated to $\mathbf{L}$, which refers to the linearized counterpart of $\boldsymbol{\mathcal{R}}$ around the current estimation of the mean flow. $\mathbf{L}$ may be expressed as

$$\mathbf{L} = \begin{pmatrix} \mathbf{L}_{uu} & \nabla\circ & \mathbf{L}_{u\tilde{\nu}} \\ \nabla\cdot\circ & 0 & 0 \\ \mathbf{L}_{\tilde{\nu}u} & 0 & \mathrm{L}_{\tilde{\nu}\tilde{\nu}} \end{pmatrix}, \tag{12}$$

with

$$\mathbf{L}_{uu} = \nabla\cdot\left(\bar{\boldsymbol{u}}\otimes\circ + \circ\otimes\bar{\boldsymbol{u}} - 2(Re^{-1}+\nu_t)\mathbf{S}(\circ)\right),\ \mathbf{L}_{u\tilde{\nu}} = \nabla\cdot\left(-2\circ\frac{\partial\nu_t}{\partial\bar{\tilde{\nu}}}\mathbf{S}(\bar{\boldsymbol{u}})\right), \tag{13}$$

$$\mathbf{L}_{\tilde{\nu}u} = (\circ\cdot\nabla)\bar{\nu} - \frac{\partial s}{\partial\bar{\boldsymbol{u}}}\cdot\circ,\ \mathrm{L}_{\tilde{\nu}\tilde{\nu}} = (\bar{\boldsymbol{u}}\cdot\nabla)\circ - \nabla\cdot(\eta\nabla\circ) - \nabla\cdot(\circ\frac{\partial\eta}{\partial\bar{\tilde{\nu}}}\nabla\bar{\tilde{\nu}}) - \frac{\partial s}{\partial\bar{\tilde{\nu}}}\circ - \frac{\partial f_{\tilde{\nu}}}{\partial\bar{\tilde{\nu}}}\circ. \tag{14}$$

From the adjoint state $\bar{\boldsymbol{q}}^\dagger$, the gradient of the cost function J with respect to the control vector g may be computed according to

$$\frac{dJ}{dg} = \bar{\tilde{\nu}}^\dagger\bar{\tilde{\nu}}^2 + \beta g. \tag{15}$$

2.2.3 Summary of the minimization procedure

The iterative data assimilation procedure may be summarized as follows. Starting with a first-guess for g, which corresponds to the baseline Spalart-Allmaras model, i.e. $g = f_{\tilde{\nu}} = 0$, the RANS equations (7) have first to be solved to get the corresponding mean flow $\bar{\boldsymbol{q}}$. This allows to solve the adjoint problem (11) and obtain the adjoint state $\bar{\boldsymbol{q}}^\dagger$. From the latter, the gradient of J with respect to g is evaluated according to (15). This gradient is then used to update the estimation of g according to the low-memory Broyden–Fletcher–Goldfarb–Shanno (L-BFGS) method [42]. A new iteration of the optimization procedure may then be performed, starting with the computation of $\bar{\boldsymbol{q}}$, until convergence is reached. More details may be found in [17,37,38]. The output of such a procedure will be referred to as the assimilated flow in the following.

The determination of an appropriate value for the weighting coefficient β in front of the penalization term in (10) is achieved through the L-curve technique [20] with an accuracy of half a decade (on a logarithmic scale), typically spanning half a dozen values around a first-guess value that is based on a preliminary data-assimilation procedure.

2.3 Linear approaches for the identification of coherent fluctuations

2.3.1 Governing equations for coherent fluctuations: perturbed and frozen eddy-viscosity approaches

Based on the mean flow and corrected RANS equations that are obtained through the above data assimilation procedure, the characterization of coherent fluctuations is now addressed through linear mean-flow analyses, thus still relying on

the hypothesis of small fluctuations $\boldsymbol{q}'$ compared to the mean flow $\bar{\boldsymbol{q}}$. In a first approach, the governing equations for $\boldsymbol{q}'$ may be obtained through a full linearization of those for the coherent flow in (5) [13,33], including perturbations in the turbulent eddy-viscosity [69,52], which will be referred to as the perturbed eddy-viscosity approach in the following. In this case, the equations for $\boldsymbol{q}'$ may be written as

$$\mathbf{B}\frac{\partial \boldsymbol{q}'}{\partial t} + \mathbf{L}\boldsymbol{q}' = \mathbf{P}\boldsymbol{f}', \quad \boldsymbol{q}' = \left(\boldsymbol{u}'^{\mathrm{T}}, \Pi', \tilde{\nu}'\right)^{\mathrm{T}}, \quad \mathbf{P} = (\mathbf{I}\,0\,0)^{\mathrm{T}}, \tag{16}$$

where the operator $\mathbf{L}$ is given in (12). Equation (16) involves a forcing $\boldsymbol{f}'$ in the momentum equations, which is considered in resolvent analysis as detailed in the following and may be interpreted as omitted nonlinear terms.

A second approach, which is commonly used in the recent literature [39,47,25, 62], consists in neglecting perturbations in the turbulent eddy-viscosity ν_t due to coherent fluctuations, avoiding the need of a turbulence model. In this so-called frozen eddy-viscosity approach, (16) is therefore simplified according to

$$\mathbf{B}_f\frac{\partial \boldsymbol{q}'_f}{\partial t} + \mathbf{L}_f\boldsymbol{q}'_f = \mathbf{P}_f\boldsymbol{f}', \quad \boldsymbol{q}'_f = \left(\boldsymbol{u}'^{\mathrm{T}}, \Pi'\right)^{\mathrm{T}}, \tag{17}$$

with

$$\mathbf{L}_f = \begin{pmatrix} \mathbf{L}_{uu} & \nabla\circ \\ \nabla\cdot\circ & 0 \end{pmatrix}, \quad \mathbf{B}_f = \begin{pmatrix} \mathbf{I} & 0 \\ 0 & 0 \end{pmatrix}, \quad \mathbf{P}_f = (\mathbf{I}\,0)^{\mathrm{T}}, \tag{18}$$

where $\mathbf{L}_{uu}$ is defined in (13). In this study, the use of the perturbed and frozen eddy-viscosity approaches (16) and (17) in the following linear analyses will be compared to assess the importance of the turbulence model in the correct estimation of coherent fluctuations.

2.3.2 Global stability analysis

Based on unforced ($\boldsymbol{f}' = \mathbf{0}$) equations (16) or (17), a first approach for characterizing coherent fluctuations may consist in performing global mean-flow stability analysis [4,58]. Considering the perturbed eddy-viscosity case (16), this amounts to investigate complex fluctuations $\boldsymbol{q}'$ of the form

$$\boldsymbol{q}'(\boldsymbol{x}, t) = \hat{\boldsymbol{q}}(\boldsymbol{x})e^{\mu t}, \quad \mu = \sigma + \mathrm{i}\omega, \tag{19}$$

where $\hat{\boldsymbol{q}}$ may be referred to as global mode, while σ and ω correspond to the growth rate and angular frequency of the mode, respectively. The mode $\hat{\boldsymbol{q}}$ is solution of the eigenvalue problem

$$-\mathbf{L}\hat{\boldsymbol{q}} = \mu\mathbf{B}\hat{\boldsymbol{q}}. \tag{20}$$

Very similarly, considering the frozen eddy-viscosity case amounts to solve the eigenvalue problem $-\mathbf{L}_f\hat{\boldsymbol{q}}_f = \mu\mathbf{B}_f\hat{\boldsymbol{q}}_f$.

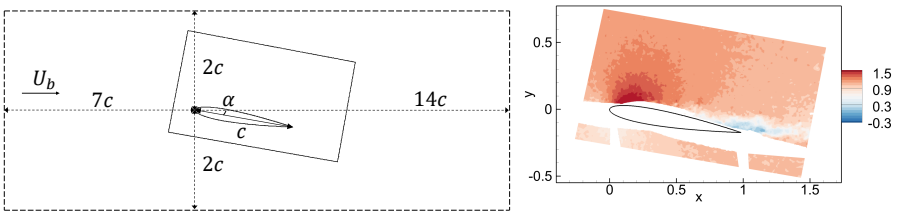

(a) (b)

Fig. 1: (a) Schematic of the experimental and numerical setups for the flow around a NACA0012 airfoil at angle of attack $\alpha = 10°$. The inner domain that is delineated by full lines corresponds to the region where planar PIV measurements are performed. The PIV measurement plane is further illustrated in (b), reporting an instantaneous snapshot of the streamwise velocity at $Re = 5.4 \cdot 10^4$. All quantities are already non-dimensionalized based on the airfoil chord length c and the incoming velocity U_b in (b), the white area corresponds to locations where no data are available. The outer domain that is delineated by dashed lines in (a) refers to the numerical domain. Still in (a), the proportions of the PIV measurement domain with respect to c are correct, while those of the numerical domain are not.

2.3.3 Resolvent analysis

As an alternative to mean-flow stability analysis, one may consider resolvent analysis [32,6], where we study the response to harmonic forcing in (16) or (17). Considering the perturbed eddy-viscosity case, $\boldsymbol{f}'$ and the flow state for coherent fluctuations $\boldsymbol{q}'$ are expressed for angular frequency ω as

$$\boldsymbol{f}'(\boldsymbol{x},t) = \hat{\boldsymbol{f}}(\boldsymbol{x})e^{\mathrm{i}\omega t}, \quad \boldsymbol{q}'(\boldsymbol{x},t) = \hat{\boldsymbol{q}}(\boldsymbol{x})e^{\mathrm{i}\omega t}. \tag{21}$$

Focusing on velocity fluctuation modes $\hat{\boldsymbol{u}}$, the latter are related to forcing modes according to

$$\hat{\boldsymbol{u}} = \mathbf{R}\hat{\boldsymbol{f}}, \quad \mathbf{R} = \mathbf{P}^{\mathrm{T}} \left(\mathrm{i}\omega\mathbf{B} + \mathbf{L}\right)^{-1} \mathbf{P}, \tag{22}$$

where $\mathbf{R}$ corresponds to the resolvent operator. Of interest for the characterization of coherent fluctuations is the computation of forcing modes $\hat{\boldsymbol{f}}$ that induce the largest responses $\hat{\boldsymbol{u}}$. This may be formulated as the maximization of the gain $\lambda^2 = \|\hat{\boldsymbol{u}}\|^2/\|\hat{\boldsymbol{f}}\|^2$ with respect to $\hat{\boldsymbol{f}}$. Choosing the norm $\|\circ\|$ as based on the usual $L^2(\Omega)$ scalar product, this amounts to solving for the following eigenvalue problem

$$\mathbf{R}^{\dagger}\mathbf{R}\hat{\boldsymbol{f}} = \lambda^2\hat{\boldsymbol{f}}, \tag{23}$$

where $\mathbf{R}^{\dagger}$ is the adjoint of $\mathbf{R}$. In the frozen eddy-viscosity case, one considers the resolvent operator $\mathbf{R}_f = \mathbf{P}_f^{\mathrm{T}} \left(\mathrm{i}\omega\mathbf{B}_f + \mathbf{L}_f\right)^{-1} \mathbf{P}_f$ instead of $\mathbf{R}$.

3 Experimental and numerical setups

3.1 Flow configuration, experimental setup and PIV measurements

We consider the experimental flow around a NACA0012 airfoil in a low-speed hydrodynamic tunnel at ONERA's Lille center. The length of the test section is 1 m,

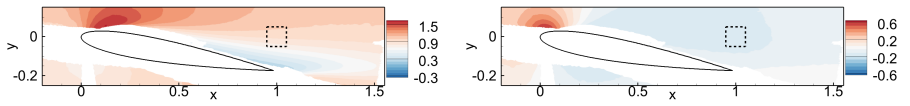

(a) (b)

Fig. 2: Mean (a) streamwise and (b) cross-stream velocities from PIV at $Re = 5.4{\cdot}10^4$. The dashed line delineates the measurement subdomain that is considered in the data-assimilation procedure in figure 10.

and its cross-section is a square of size 0.3 m. The NACA0012 airfoil, whose chord length is $c = 0.075\,\mathrm{m}$, is positioned over the entire width of the test section with an angle of attack of $\alpha = 10°$. The incoming velocity upstream of the airfoil U_b is varied between $0.57\,\mathrm{m\cdot s^{-1}}$ and $0.85\,\mathrm{m\cdot s^{-1}}$, which leads to a chord-based Reynolds number $Re = U_b c/\nu$, where ν refers to water kinematic viscosity, between $4.3 \cdot 10^4$ and $6.4 \cdot 10^4$. In previous section, as in the following, all non-dimensional quantities are non-dimensionalized based on U_b and c. In particular, we will consider non-dimensional frequencies that are defined as $St = fc/U_b$ (where f refers to a dimensional frequency).

Double-frame (thus non-time-resolved) planar PIV measurements are acquired in a longitudinal plane at mid-span of the airfoil, which is illustrated in figure 1. They are performed thanks to two Phantom V710 cameras. The flow is illuminated with a Quantronix Darwin-Duo Nd:YLF pulsed laser from above of the suction side of the airfoil. Particle image doublets are acquired at a frequency rate of 100 Hz during 50 s (the frequency between the two pulses to acquire an image doublet is 1 kHz). 5000 image doublets are thus obtained, in a single run, for each investigated value of U_b. The time resolution of the present PIV measurements corresponds to a maximal acquirable non-dimensional frequency that verifies $4.4 \leq St_{\max} \leq 6.6$ according to Nyquist criterion for the present range of investigated U_b, while the total duration of the PIV acquisition corresponds to a minimum frequency that lies in the range $1.8 \cdot 10^{-3} \leq St_{\min} \leq 2.6 \cdot 10^{-3}$. PIV vector fields are obtained from the particle image doublets based on ONERA's software FOLKI-SPIV. The later relies on a multi-resolution approach where a Lucas-Kanade algorithm [2] is employed to sequentially compute displacements from progressively less low-pass filtered versions of the original images. More details may be found in [12]. We rely on square interrogation windows with a size of 15 pixels. As a uniform weighting is employed in the interrogation windows, PIV processing can be considered at first approximation as a top hat filtering of the true flow in the latter. With a camera calibration of 8 pixels·mm^{-1}, the size of the interrogation windows, and thus that associated to the PIV filtering effect, corresponds to a non-dimensional length of 0.025. Finally, it may be mentioned that the airfoil and the calibration plate for the PIV system were mounted on the same support, allowing to identify the physical location of the airfoil in the PIV fields.

An instantaneous PIV snapshot at $Re = 5.4 \cdot 10^4$ and the mean flow that is obtained through time-average of such snapshots are illustrated in figures 1b and 2, respectively. The white area in the figures corresponds to regions where no data are available due to the local average cross-correlation coefficient between matched image intensity values [48] being less than 0.33 in average, a value that

has been chosen as relevant for the present signal-to-noise conditions. In particular, no information is available on the pressure side of the airfoil, nor on the suction side close to the leading edge. Note that these unavailable zones partly correspond to the presence of intense flow gradients, but also to laser light reflections or background perturbations, which remain in the images. In the present processing, these difficulties have already been addressed using a traditional pre-processing step of background subtraction. More advanced approaches, such as POD-based filtering [34], could possibly help in further mitigating these effects; their evaluation is the purpose of future work on the data. In the end, the mean velocity field as reported in figure 2 thus remains inaccessible over a large part of the airfoil through PIV in the present case. This prevents from relying on such an experimental mean flow to directly perform linear mean-flow analyses, which is expected to be a common situation in the case of turbulent flows in the presence of wall boundaries.

Such a time-averaged experimental velocity field forms the measurements $\bar{\boldsymbol{m}}$ in the data assimilation procedure of §2.2. The associated observation operator $\mathbf{H}$ may be decomposed as

$$\mathbf{H} = \mathbf{F}\mathbf{P}^{\mathrm{T}}, \tag{24}$$

where the application of $\mathbf{P}^{\mathrm{T}}$ (see (16)) to a full mean flow $\bar{\boldsymbol{q}}$ allows to extract its velocity components (i.e. $\mathbf{P}^{\mathrm{T}}\bar{\boldsymbol{q}} = \bar{\boldsymbol{u}}$), while $\mathbf{F}$ applies the above-described filtering operation that mimics PIV processing, namely top-hat filtering with a square support of size 0.025. After spatial discretization (see §3.2), the discrete counterpart of $\mathbf{F}$ will be a matrix whose elements correspond to the filter kernel, taking into account quadrature weights. The scalar product for the measurement space that is involved in the measurement term J_m of the cost function in (9) corresponds to the standard $L^2(\Omega_m)$ one, where Ω_m refers to either the full PIV plane or only the subdomain that is delineated by dashed lines in figure 2. The measurement term J_m may therefore be expressed as

$$J_m = \int_{\Omega_m} (\mathbf{F}\bar{\boldsymbol{u}} - \bar{\boldsymbol{m}})^{\mathrm{T}} (\mathbf{F}\bar{\boldsymbol{u}} - \bar{\boldsymbol{m}}) \, d\Omega_m. \tag{25}$$

3.2 Numerical implementation and RANS results

The spatial discretization of the RANS operator $\boldsymbol{\mathcal{R}}$ in (6) and of its linearized counterparts in (12) and (18) is performed with the finite-element method as implemented in the software FreeFEM [22]. Second-order polynomial elements are employed for velocity components, while pressure and eddy-viscosity variables are discretized with piecewise-linear functions. Streamline-upwind Petrov–Galerkin (SUPG) [9] and grad–div [44] stabilizations are employed to tackle the considered relatively high-Reynolds-number flows. The two-dimensional rectangular computational domain is chosen to have similar extents to that of the hydrodynamic tunnel, namely $[-7, 14] \times [-2, 2]$, as reported in figure 1a. This domain is discretized through an unstructured mesh that is formed of around $5 \cdot 10^4$ triangles whose distribution is obtained by an automatic adaptation procedure based on the Hessian of the velocity, pressure and eddy-viscosity fields, and also of the sensitivity fields that are discussed in §4.2, ensuring the mesh-convergence of the data-assimilation

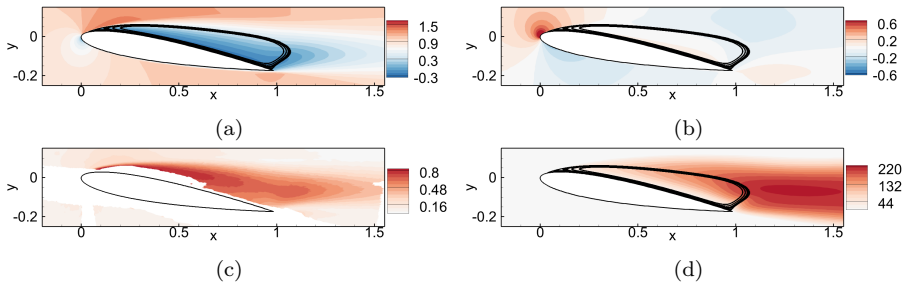

Fig. 3: Baseline RANS results at $Re = 5.4 \cdot 10^4$: mean (a) streamwise and (b) cross-stream velocities, (c) error field e_m in (26) and (d) turbulent eddy-viscosity field ν_t multiplied by Re. Black lines in (a,b,d) correspond to streamlines that delineate the recirculation region.

results and of those of the linear mean-flow analyses. Such a mesh adaption procedure also minimizes the importance of the SUPG and grad-div stabilizations in important flow regions, as the (local) stabilization parameters scale quadratically with the size of the elements, which is automatically reduced in high-gradient regions through the mesh adaption. As such, stabilization mainly acts in freestream regions, where relatively large elements may be employed. The nonlinearity of the RANS equations in (7) is tackled through the Newton method, which involves the inversion of their linearized counterpart $\mathbf{L}$ in (12). Boundary conditions for the RANS equations are as follows. At the inlet, streamwise and cross-stream velocity components are set to $\bar{u} = 1$ and $\bar{v} = 0$, respectively, while $\bar{\tilde{\nu}} = 0.02Re^{-1}$ is imposed [41]. No-slip conditions $\bar{\boldsymbol{u}} = \mathbf{0}$ are enforced at the airfoil surface in conjunction with $\bar{\tilde{\nu}} = 0$. Symmetry conditions are imposed at top and bottom boundaries, namely $\frac{\partial \bar{u}}{\partial y} = \frac{\partial \bar{\tilde{\nu}}}{\partial y} = \bar{v} = 0$. Finally, $\frac{\partial \bar{\tilde{\nu}}}{\partial x} = 0$ and $2(Re^{-1} + \nu_t)\mathbf{S}(\bar{\boldsymbol{u}}) \cdot \boldsymbol{n} - \bar{\Pi}\boldsymbol{n} = \mathbf{0}$ are used at the outlet, where $\boldsymbol{n}$ denotes the normal vector. Adjoint operators, such as involved in (11), are derived following a discrete approach [46]. Namely, as an example, the adjoint RANS operator $\mathbf{L}^\dagger$ is obtained by taking the transpose of the discretized counterpart of $\mathbf{L}$. For the same reasons as outlined above, the employed stabilizations schemes do not significantly affect the adjoint operator in important flow regions. Both direct and adjoint problems are solved in a parallel way relying on the PETSc library [3], more details about its interface with FreeFEM may be found in [40]. Eigenvalue problems as involved in (20) and (23) are solved based on the software ARPACK [27] as interfaced with FreeFEM.

The mean velocity field that is solution of the baseline RANS equations is illustrated in figures 3a-3b for $Re = 5.4 \cdot 10^4$. It appears significantly more detached than the PIV field in figure 2 with a large recirculation region. The significant discrepancies between the PIV and RANS mean-velocity fields are further illustrated through figure 3c, which reports the error field e_m defined as

$$e_m(\boldsymbol{x}) = \left((\mathbf{F}\bar{\boldsymbol{u}} - \bar{\boldsymbol{m}})^{\mathrm{T}} (\mathbf{F}\bar{\boldsymbol{u}} - \bar{\boldsymbol{m}}) \right)^{\frac{1}{2}}. \tag{26}$$

It may noted that e_m^2 corresponds to the integrand in the measurement term J_m in (25). This field takes values that are close to 1, i.e. of the same order of magnitude as the incoming velocity, in a significant part of the measurement domain,

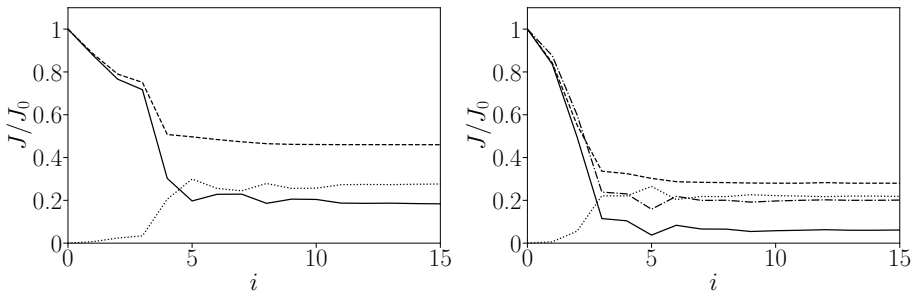

Fig. 4: Cost function J in (9) normalized by its initial value J_0 (dashed lines) versus the iteration i of the data assimilation procedure when considering the PIV mean-velocity field at $Re = 5.4 \cdot 10^4$ (a) in the full measurement plane or (b) only in the subdomain that is delineated in dashed lines in figure 2. The contributions from the measurement term J_m/J_0 (full lines) and penalization term J_p/J_0 (dotted lines) are also reported. In (b), the discrepancies with respect to the full measurements (same definition as J_m/J_0 in (a)) are also reported through the dashed-dotted line.

confirming the large deficiencies in the employed turbulence model in correctly predicting the considered near-stall flow, as further discussed in the following.

4 Results

4.1 Data assimilation

Neither the PIV measurements nor the RANS predictions of §3 can directly be employed to characterize coherent fluctuations through the linear methodologies in §2.3 due to their incomplete character for the former and their lack of fidelity for the latter. In this section, we apply the data assimilation procedure of §2.2 to correct the Spalart-Allmaras model (4) in order to get a full mean flow that is as close as possible to the mean PIV measurements. Still considering the case $Re = 5.4 \cdot 10^4$, we first perform data assimilation relying on the full PIV mean-velocity field in figure 2, thus evaluating the measurement term J_m in (25) with Ω_m corresponding to the full PIV plane. The corresponding evolution of the cost function J defined in (9) along the iteration of the data assimilation procedure is reported in figure 4a with the dashed line. The contributions from the measurement term J_m and the penalization one J_p are reported with solid and dotted lines, respectively. Results are normalized with the value of J at the beginning of the data assimilation procedure, which is denoted by J_0 and thus corresponds to the evaluation of J for baseline RANS. The convergence of data assimilation is reached in 15 iterations, which remains moderate for such a procedure. It appears that the value of the measurement term J_m has been divided by a factor of roughly 5, indicating a significant improvement in the assimilated RANS mean flow compared to the baseline one.

The mean velocity field for the corresponding assimilated RANS solution, which is illustrated in figures 5a-5b, is significantly altered from the baseline solu-

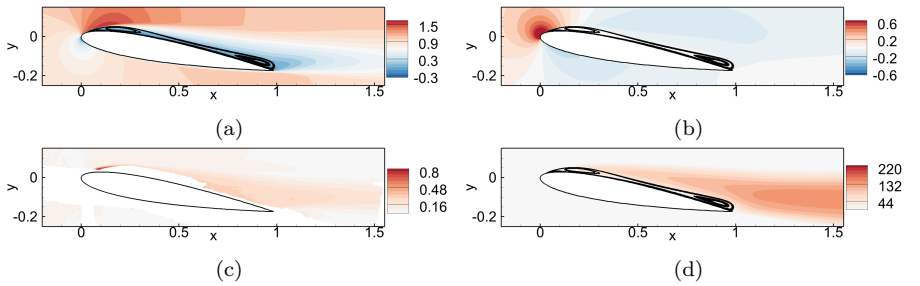

Fig. 5: Assimilated RANS results at $Re = 5.4 \cdot 10^4$ based on the full PIV mean-velocity field: mean (a) streamwise and (b) cross-stream velocities, (c) error field e_m in (26) and (d) turbulent eddy-viscosity field ν_t multiplied by Re.

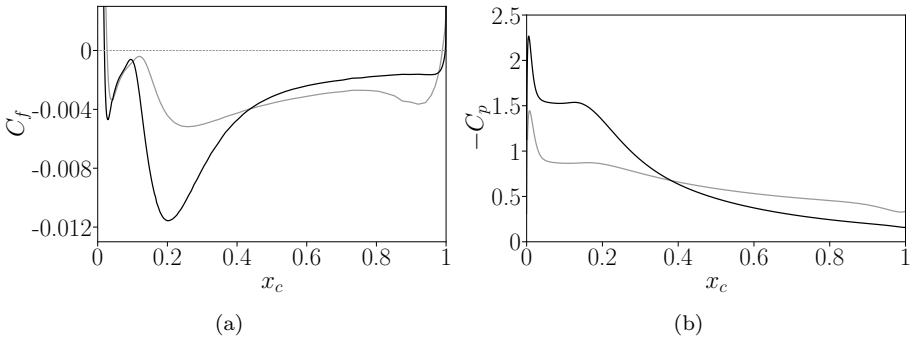

Fig. 6: (a) Skin friction and (b) pressure coefficients at the suction side for baseline (grey lines) and assimilated (black lines) RANS at $Re = 5.4 \cdot 10^4$ (based on the full PIV mean-velocity field).

tion (figures 3a-3b). Instead of the large recirculation region, a thinner recirculation region is visible on the suction side of the airfoil. It is composed of a leading-edge recirculation region and a trailing-edge one that are connected. The assimilated velocity field appears significantly closer to the PIV field (figure 2), as confirmed by the low level of remaining discrepancies that are reported in figure 5c (to compare with figure 3c). The largest remaining errors concentrate close to the airfoil and at the boundaries of the measurement domain where the cross-correlation coefficient between intensity images (see §3.1), and thus the confidence in the PIV data, is lower than in the rest of the domain. From the comparison between figures 3d and 5d, it appears that the decrease in the size of the recirculation region is associated to a lower turbulent viscosity ν_t for the assimilated solution, at least downstream of the airfoil. This is further discussed in the following. The skin-friction and pressure coefficients at the suction side of the airfoil are reported in figure 6a and 6b, respectively, to better illustrate the near-wall behavior of the mean-velocity field. The skin-friction of the assimilated solution (black curve) is negative everywhere except close to the leading-edge of the airfoil, indicating that the assimilated flow is still fully detached. The plateau in the C_p distribution, which is far more pro-

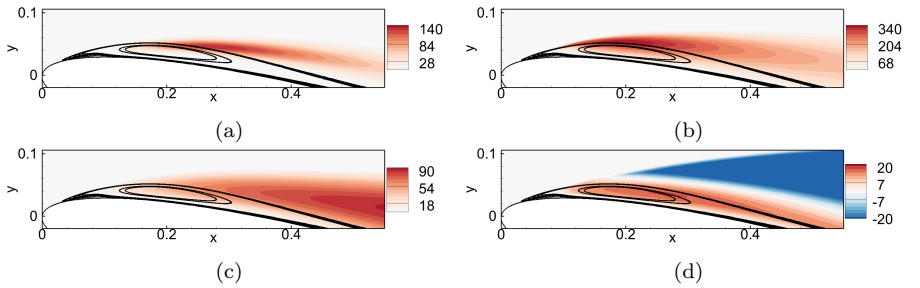

Fig. 7: (a) Model correction $f_{\tilde{\nu}} = g\bar{\tilde{\nu}}^2$, (b) production term $P_{\tilde{\nu}}$ and (c) turbulent eddy-viscosity field ν_t^a for assimilated RANS at $Re = 5.4 \cdot 10^4$ (based on the full PIV mean-velocity field); (d) variation $(\nu_t^a - \nu_t^b)$ in the turbulent eddy-viscosity between assimilated and baseline (ν_t^b) RANS. All quantities are multiplied by Re.

nounced in the assimilated flow compared to the baseline one, is characteristic of the leading-edge recirculation region.

The correction of the Spalart-Allmaras model in (4) through the data assimilation procedure is further investigated through figure 7. The assimilated turbulent eddy-viscosity field, which is reproduced in figure 7c with a zoomed view on the suction side, starts to be significant in the middle of the leading-edge recirculation region. The laminar/turbulent transition thus occurs in this leading-edge recirculation region, which is thus commonly referred to as laminar-separation bubble. The corrective field $f_{\tilde{\nu}}$ is overall positive (figure 7a), thus acting as a source of turbulent eddy-viscosity. It concentrates over the leading-edge laminar-separation bubble at locations where the production term $P_{\tilde{\nu}}$ in the Spalart-Allmaras model takes relatively high values (figure 7b). Such a correction is consistent with findings in previous studies [7] that identified the need of enhancing production in RANS models to account for strong non-equilibrium effects (production of turbulent kinetic energy largely exceeding dissipation) that occur in the transitional flow region over laminar-separation bubbles. Compared to the baseline RANS solution, figure 7d indicates that this supplementary production effect has induced a significant increase in the turbulent eddy-viscosity close to the wall (red region). This increase in eddy-viscosity contributes to (partially) reattach the turbulent separated shear layer. The latter partial reattachment induces a significant decrease in the production of eddy-viscosity outside of the boundary layer region, which corresponds to the blue region in figure 7d. This reduction in the turbulent eddy-viscosity in the assimilated solution compared to the baseline one persists downstream of the airfoil, as mentioned above and illustrated through figures 3d and 5d.

The Reynolds stress tensors as evaluated from PIV and modelled in the assimilated RANS solution are then compared through figure 8. In the case of PIV, the Reynolds stresses are estimated from the experimental flow fluctuations, namely the PIV snapshots from which the time-averaged mean has been subtracted. Such fluctuations correspond to measurements of $\tilde{\boldsymbol{u}} = \boldsymbol{u}' + \boldsymbol{u}''$, namely include both the coherent $\boldsymbol{u}'$ and turbulent $\boldsymbol{u}''$ fluctuations. The experimental normal stresses $\overline{\tilde{u}\tilde{u}}$ and $\overline{\tilde{v}\tilde{v}}$ are first reported in figures 8a and 8b, respectively. Both stresses, and therefore also the kinetic energy $\tilde{k} = \frac{1}{2}(\overline{\tilde{u}\tilde{u}} + \overline{\tilde{v}\tilde{v}})$, are mostly concentrated over the

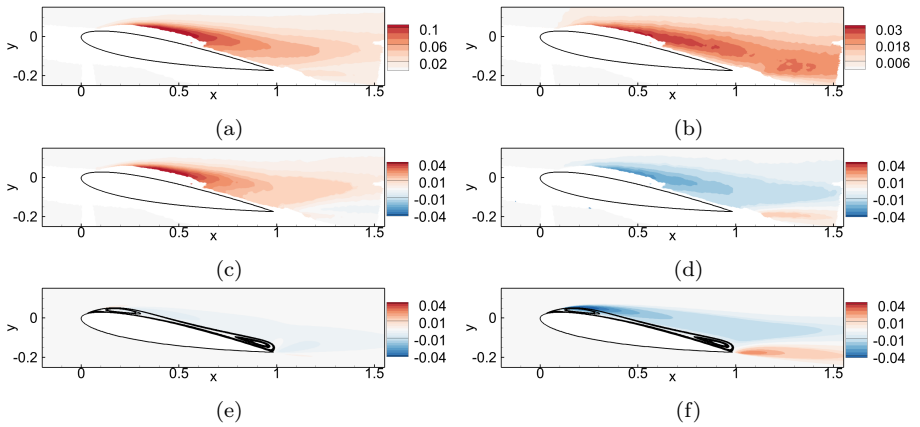

Fig. 8: (a-d) Reynolds stresses from PIV at $Re = 5.4 \cdot 10^4$: normal stresses (a) $\overline{\tilde{u}\tilde{u}}$ and (b) $\overline{\tilde{v}\tilde{v}}$, (c) deviatoric stress $\overline{\tilde{u}\tilde{u}}^{\mathrm{d}}$ and (d) shear stress $\overline{\tilde{u}\tilde{v}}$. (e-f) Reynolds stresses for the assimilated RANS solution (based on the full PIV mean-velocity field): (e) deviatoric stress $\overline{u''u''}^{\mathrm{d}}$ and (f) shear stress $\overline{u''v''}$.

first half of the suction side. The deviatoric stress $\overline{\tilde{u}\tilde{u}}^{\mathrm{d}} = \overline{\tilde{u}\tilde{u}} - \tilde{k}$ along with the shear stress $\overline{\tilde{u}\tilde{v}}$ (which is equal to its deviatoric counterpart) are also displayed in figures 8c and 8d, respectively. $\overline{\tilde{u}\tilde{u}}^{\mathrm{d}}$ is overall positive, as the normal stress $\overline{\tilde{u}\tilde{u}}$ is significantly larger than $\overline{\tilde{v}\tilde{v}}$ in a large part of the flow domain (figures 8a-8b). Conversely, the deviatoric stress $\overline{\tilde{v}\tilde{v}}^{\mathrm{d}} = -\overline{\tilde{u}\tilde{u}}^{\mathrm{d}}$ is overall negative. In the assimilated RANS results, it is worth reminding that the modelled Reynolds stress tensor is supposed to account for turbulent fluctuations $\boldsymbol{u}''$ only. In addition, the Boussinesq hypothesis only gives access to the deviatoric part of this tensor according to $\overline{\boldsymbol{u}'' \otimes \boldsymbol{u}''}^{\mathrm{d}} = -2\nu_t \mathbf{S}(\bar{\boldsymbol{u}})$. The corresponding components $\overline{u''u''}^{\mathrm{d}}$ and $\overline{u''v''}$ are illustrated in figures 8e and 8f, respectively, which may be compared with their PIV counterparts in figures 8c and 8d, respectively. The modelled shear stress $\overline{u''v''}$ (figure 8f) appears in relatively good agreement with the measured stress $\overline{\tilde{u}\tilde{v}}$ (figure 8d). On the other hand, the modelled stress $\overline{u''u''}^{\mathrm{d}}$ is negative (figure 8e) while the measured one $\overline{\tilde{u}\tilde{u}}^{\mathrm{d}}$ is positive and of much larger amplitude (figure 8c). Such discrepancies may suggest deficiencies in the Boussinesq hypothesis and possibly in the Spalart-Allmaras model for the correct representation of the Reynolds stress tensor in the present case. However, one has to keep in mind that the experimental Reynolds stresses include contributions from coherent fluctuations, while the latter are not supposed to be modelled by the Boussinesq hypothesis but rather resolved, as performed in the following through linear analyses.

What ultimately matters in the correct estimation of the mean-velocity field is the functional aspect of the turbulence model in the momentum equations (borrowing a concept in [51]), namely the divergence of the modelled Reynolds stress tensor, and more specifically the solenoidal part of this quantity [16]. Accordingly, we compute the vectors $-\nabla\cdot(\overline{\tilde{\boldsymbol{u}} \otimes \tilde{\boldsymbol{u}}})$ and $\nabla\cdot(2\nu_t \mathbf{S}(\bar{\boldsymbol{u}}))$ from the PIV and assimilated RANS results, respectively, and extract their solenoidal components following [16], which are denoted by $\bar{\boldsymbol{f}}_m$ and $\bar{\boldsymbol{f}}_a$, respectively. The latter quantities are displayed

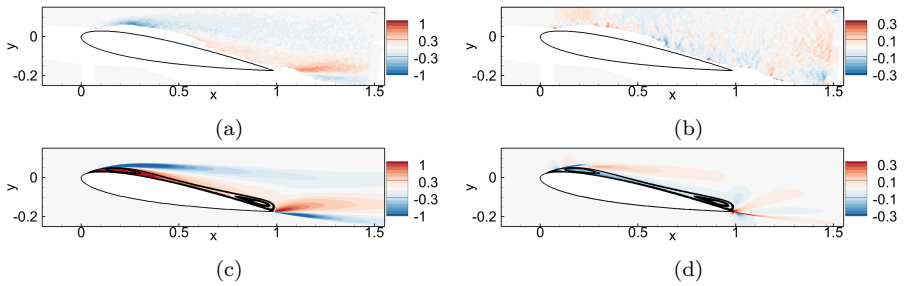

Fig. 9: Solenoidal contributions of (a,b) $-\nabla\cdot(\widetilde{\tilde{\boldsymbol{u}}\otimes\tilde{\boldsymbol{u}}})$ from the PIV results at $Re = 5.4\cdot10^4$ and of (c,d) $\nabla\cdot(2\nu_t\mathbf{S}(\bar{\boldsymbol{u}}))$ from assimilated RANS (based on the full PIV mean-velocity field). Both (a,c) streamwise and (b,d) cross-stream components of these contributions are reported.

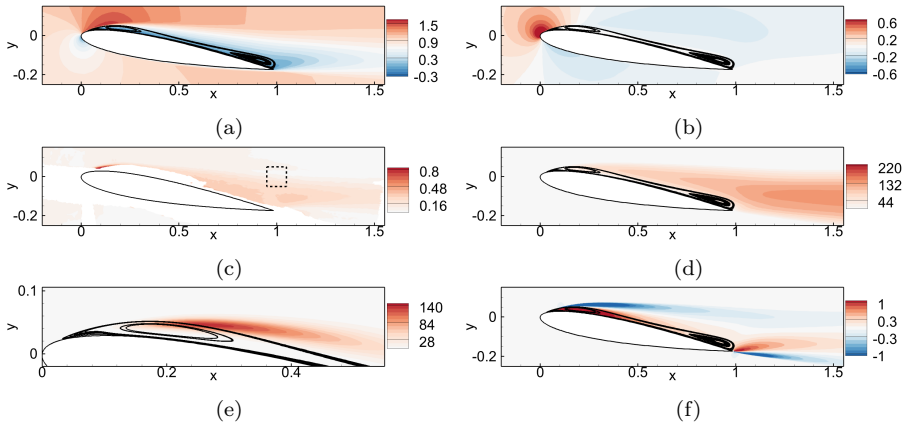

Fig. 10: Assimilated RANS results at $Re = 5.4\cdot10^4$ based on PIV mean-velocity data in the subdomain that is delineated by dashed lines in (c) and in figure 2: mean (a) streamwise and (b) cross-stream velocities, (c) error field e_m in (26), (d) turbulent eddy-viscosity field ν_t, (e) model correction $f_{\tilde{\nu}} = g\bar{\tilde{\nu}}^2$ and (f) streamwise component of the solenoidal part of $\nabla\cdot(2\nu_t\mathbf{S}(\bar{\boldsymbol{u}}))$.

in figure 9. The streamwise components of $\bar{\boldsymbol{f}}_m$ (figure 9a) and $\bar{\boldsymbol{f}}_a$ (figure 9c) are very similar. Comparing their cross-stream components is more difficult as they are of smaller amplitude and the experimental estimate is thus relatively more affected by the non-smooth character of the PIV data (figure 9b). Besides, the cross-stream component of $\bar{\boldsymbol{f}}_a$ mostly concentrates in regions that are inaccessible in the PIV measurements close to the leading and trailing edges (figure 9d). Still, figure 9 confirms the ability of the data assimilation procedure in correctly adjusting the turbulence model to reproduce the action of the Reynolds stress tensor in the momentum equations.

Finally in this section, we investigate the possibility in relying on very limited data to infer a reliable mean-flow description. Figures 4b and 10 report data-assimilation results when considering the PIV mean-velocity field only in the sub-

domain that is delineated by dashed lines in figures 2 and 10c. The domain Ω_m that is involved in the evaluation of the measurement term J_m in (25) thus corresponds to this subdomain in the present case. The corresponding convergence of the data-assimilation procedure is illustrated in figure 4b. It is achieved as quickly as in the full measurement case (figure 4a). The measurement term J_m and the full cost function J reach here lower values, which may be attributed not only to the lower dimension of the measurement space in this case but also to the location of this measurement subdomain in a flow region relatively far from the airfoil's wall where the PIV data are more trustworthy. This was quantified through higher values of the cross-correlation coefficient between matched image intensities in the considered measurement subdomain compared to locations that are closer to the airfoil's wall. The discrepancies with respect to the full PIV mean-velocity field are quantified through (25) with Ω_m chosen as the full PIV plane, which corresponds to the same definition as for the measurement term J_m in the full measurement case (full line in figure 4a). They are reported through the dashed-dotted line in figure 4b. Remarkably, the discrepancies with respect to the full PIV field are almost reduced as much in the present case as when these full measurements are used in the data-assimilation procedure. This is further illustrated by the high degree of similarity between the assimilated mean flows in the present partial measurement case (figure 10) and in the full measurement one (figures 5, 7a and 9c). In particular, it is striking that the data assimilation procedure has identified a similar model correction that concentrates over the leading-edge laminar-separation bubble in the partial measurement case (figure 10e). Only small differences between the two assimilated mean-velocity fields may be identified close to the trailing edge, translating into slightly larger errors compared the PIV data in this region in the partial measurement case (figure 10c) compared to the full measurement one (figure 5c). The present results therefore support the robustness of the data-assimilation procedure with respect to the sparse character of the considered measurements, which may be encouraging for the application of the present methodology to other configurations. In the following, we will only rely on the assimilated solution that has been obtained based on the full PIV mean-velocity field for the application of the linear methodologies in §2.3.

4.2 Global stability analysis

As a first step to characterize coherent fluctuations relying on the previously-obtained assimilated RANS solution (based on the full PIV mean-velocity field), we perform mean-flow stability analysis as described in §2.3.2. The eigenvalue spectra that are obtained with the perturbed and frozen eddy-viscosity approaches (see §2.3.1) are displayed in figures 11a-11b through black and grey circles, respectively. It appears that taking into account or not perturbations in the turbulent eddy-viscosity has a significant impact on stability results at low frequencies St (figure 11b). In the frozen eddy-viscosity approach, a steady mode ($St = 0$), which is highlighted with the open red circle, is found unstable ($\sigma > 0$). The corresponding spatial structure is reported in figure 11c. It may be noted that this mode is real as the associated frequency is 0. In the perturbed eddy-viscosity approach, all modes are stable but the least stable mode (denoted with a red filled circle, and its complex conjugate) is now unsteady and associated to the non-dimensional frequency

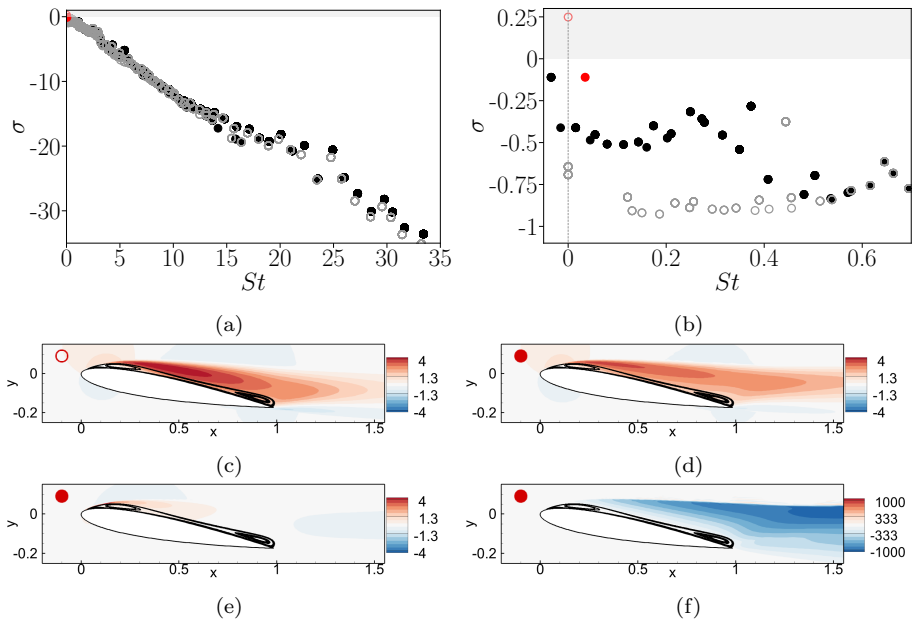

Fig. 11: First row: (a) eigenvalue $\mu = \sigma + \mathrm{i}2\pi St$ spectrum for the assimilated flow at $Re = 5.4{\cdot}10^4$ in the perturbed (filled black circles) or frozen (empty grey circles) eddy-viscosity approach, (b) zoomed view around small St. The (real) streamwise velocity component for the unstable mode in the frozen approach (empty red circle in (a,b)) is reported in (c). The least stable mode in the perturbed approach (full red circle in (a,b)) is illustrated through the (d) real and (e) imaginary parts of its streamwise velocity component and (f) the real part of its eddy-viscosity.

$St = 0.035$. The real and imaginary parts of the streamwise velocity component for this low-frequency mode are illustrated in figures 11d-11e. They correspond to large-scale velocity perturbations over the whole suction side. When superimposed to the mean-flow, this mode would induce an oscillation between attached (high lift) and detached (low lift) flow states. The eddy-viscosity component of this mode, which mostly concentrates downstream of the airfoil and close to the shear layer that originates from the leading edge, is also reported in figure 11f. Similar low-frequency modes have been identified by [24] and [10] for airfoils in near-stall conditions, but in fully turbulent regimes at much higher Reynolds numbers ($Re > 10^6$). For the lower Reynolds number regime that is investigated in the present study, these low-frequency modes are identified for the first time through stability analysis, to the authors' knowledge. On the other hand, the identified frequency $St = 0.035$ is close to that estimated in large-eddy simulations of flows past NACA0012 airfoils in conditions that are close to the present ones. Among others, [36] and [15] have reported low-frequency flow oscillations of a similar nature around $St = 0.033$ and $St = 0.045$, respectively, at $Re = 5 \cdot 10^4$ and for angles of attack similar or equal to the present one ($\alpha = 9.4°$ and $\alpha = 10°$, respectively), and at low but non-zero Mach numbers ($Ma = 0.3$ and $Ma = 0.4$, respectively).

$\delta\mathbf{L}$	$\mathbf{L}_{\mathrm{N}u}$	$\mathbf{L}_{\mathrm{N}\tilde{\nu}}$	$\mathbf{L}_{\mathrm{S}}$
$\delta\sigma/\lvert\sigma\rvert$	2.51	-3.95	0.44
$\delta\omega/\lvert\omega\rvert$	-0.13	1.38	-0.25

Table 1: Relative contribution of various components $\delta\mathbf{L}$ of the linearized RANS equations (see (29)) to the growth rate σ and angular frequency ω of the least stable mode in the perturbed eddy-viscosity approach (figures 11d-11f) as evaluated through (27).

In order to provide further insight into the above-discussed low-frequency mode identified in perturbed eddy-viscosity approach and the importance of the turbulence model in its estimation, we perform sensitivity analysis of the stability results following the endogeneity approach discussed in [30,45]. At first order, the eigenvalue variation $\delta\mu$ associated to any global mode $\hat{\boldsymbol{q}}$ that is induced by the operator variation $\delta\mathbf{L}$ in the linearized RANS equations may be evaluated according to

$$\delta\mu = \delta\sigma + \mathrm{i}\delta\omega = \left\langle \hat{\boldsymbol{q}}^\dagger, -\delta\mathbf{L}\hat{\boldsymbol{q}} \right\rangle = \int_\Omega -\hat{\boldsymbol{q}}^{\dagger\,\mathrm{H}} \delta\mathbf{L}\hat{\boldsymbol{q}}\, d\Omega, \tag{27}$$

where $\circ^{\mathrm{H}}$ denotes the Hermitian transpose, and $\hat{\boldsymbol{q}}^\dagger$ is the associated adjoint mode that verifies

$$-\mathbf{L}^\dagger\hat{\boldsymbol{q}}^\dagger = \mu^{\mathrm{H}}\mathbf{B}\hat{\boldsymbol{q}}^\dagger, \quad \left\langle \hat{\boldsymbol{q}}^\dagger, \mathbf{B}\hat{\boldsymbol{q}} \right\rangle = 1. \tag{28}$$

Considering $\delta\mathbf{L} = \mathbf{L}$ in (27) leads to $\delta\mu = \mu$, so that the integrand $-\hat{\boldsymbol{q}}^{\dagger\,\mathrm{H}}\mathbf{L}\hat{\boldsymbol{q}}$ may be interpreted as the local contribution of $\mathbf{L}$ to the eigenvalue μ [30]. A deeper analysis may consist in choosing $\delta\mathbf{L}$ as components of $\mathbf{L}$ in order to disentangle their respective importance in the stability results. Accordingly, we consider the following possibilities for $\delta\mathbf{L}$

$$\mathbf{L}_{\mathrm{N}u} = \begin{pmatrix} \mathbf{L}_{uu} & \nabla\circ & 0 \\ \nabla\cdot\circ & 0 & 0 \\ 0 & 0 & 0 \end{pmatrix}, \mathbf{L}_{\mathrm{N}\tilde{\nu}} = \begin{pmatrix} 0 & 0 & \mathbf{L}_{u\tilde{\nu}} \\ 0 & 0 & 0 \\ 0 & 0 & 0 \end{pmatrix}, \mathbf{L}_{\mathrm{S}} = \begin{pmatrix} 0 & 0 & 0 \\ 0 & 0 & 0 \\ \mathrm{L}_{\tilde{\nu}u} & 0 & \mathrm{L}_{\tilde{\nu}\tilde{\nu}} \end{pmatrix}. \tag{29}$$

The first two choices allow to assess the contribution of the momentum and continuity equations in the eigenvalue μ, distinguishing between contributions that account for velocity and pressure fluctuations only ($\delta\mathbf{L} = \mathbf{L}_{\mathrm{N}u}$), similarly as in the frozen eddy-viscosity approach, and the contribution from varying turbulent eddy-viscosity in the momentum equations ($\delta\mathbf{L} = \mathbf{L}_{\mathrm{N}\tilde{\nu}}$). The third choice allows to identify the direct influence of the linearized Spalart-Allmaras equation on the stability results ($\delta\mathbf{L} = \mathbf{L}_{\mathrm{S}}$). It may be noted that $\mathbf{L} = \mathbf{L}_{\mathrm{N}u} + \mathbf{L}_{\mathrm{N}\tilde{\nu}} + \mathbf{L}_{\mathrm{S}}$. Therefore, when evaluating (27) for the three above choices of $\delta\mathbf{L}$, and summing the results, one recovers μ. Table 1 reports such an analysis for the above-discussed low-frequency mode. This table first shows that the direct impact of the linearized Spalart-Allmaras equation (column $\mathbf{L}_{\mathrm{S}}$) on the growth rate and frequency of this mode is of secondary importance. On the other hand, the values that are reported in the column $\mathbf{L}_{\mathrm{N}\tilde{\nu}}$ show not only the stabilizing effect of taking into account perturbations of the turbulent eddy-viscosity in the momentum equations, but also the primary importance of the latter in the value of the frequency. These results appear in line with the previous comparison between the frozen and perturbed eddy-viscosity approaches.

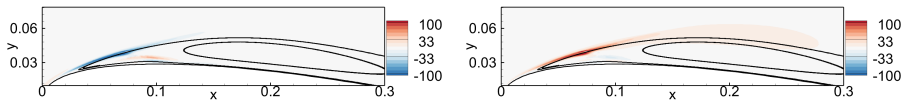

Fig. 12: Local contribution to the (a) growth rate σ and (b) angular frequency ω of the least stable mode in the perturbed eddy-viscosity approach (figures 11d-11f) from momentum and continuity equations (integrand in (27) with $\delta\mathbf{L} = \mathbf{L}_{\mathrm{N}u} + \mathbf{L}_{\mathrm{N}\tilde{\nu}}$).

As mentioned above, the endogeneity analysis also allows to identify flow regions that strongly contribute to the growth rate and frequency of an eigenmode by examining the integrand of (27). By specifically considering the operator variation $\delta\mathbf{L} = \mathbf{L}_{\mathrm{N}u} + \mathbf{L}_{\mathrm{N}\tilde{\nu}}$, we identify the (prevailing) local contribution of the momentum and continuity equations to the eigenvalue μ. This is illustrated in figure 12 for the present low-frequency mode, distinguishing between contributions to the growth rate and angular frequency. In both cases, the corresponding fields are highly concentrated in the upstream part of the leading-edge laminar-separation bubble, highlighting the crucial role of the latter in the considered low-frequency phenomena. It may be noted that the flow is laminar in this region as the latter is associated to small values for the turbulent eddy-viscosity field (figure 7c), while the present assimilated turbulence-modelling correction acts downstream of this sensitive region (figure 7a). This makes stability results robust with respect to small changes in the identified correction, which is not the case for other choices of model correction, as detailed in appendix B.

4.3 Resolvent analysis and comparison with SPOD results

As the above-discussed assimilated mean-flow is stable, at least in the perturbed eddy-viscosity approach, it is worth performing resolvent analysis as described in §2.3.3 to investigate how exogenous forcing may sustain the identified low-frequency flow oscillations. Moreover, in both perturbed and frozen eddy-viscosity approaches, the present global stability analysis results do not allow to easily identify any coherent fluctuations that may arise at higher frequencies, such as vortex-shedding or Kelvin-Helmholtz phenomena, since all these frequencies are strongly stable. This also motivates the use of resolvent analysis to characterize such phenomena, as performed in [66, 67, 72, 63, 71, 29] based on the linearization of the (laminar) Navier-Stokes equations, while we here thus rely on RANS modelling to introduce a distinction between turbulent and coherent scales.

Resolvent analysis results are first illustrated through figure 13a, which reports the first and second largest gains λ^2 as functions of the non-dimensional frequency St as obtained in the perturbed (black curves) and frozen (grey curves) eddy-viscosity approaches. It may be noted that the subdominant gains (reported through dash-dotted lines) in the perturbed and frozen approaches are nearly identical, so that the corresponding curves overlap. Starting by considering the low-frequency range $St \lesssim 0.1$, no particular amplification is predicted in the frozen eddy-viscosity approach, as first and second gains are of the same magnitude.

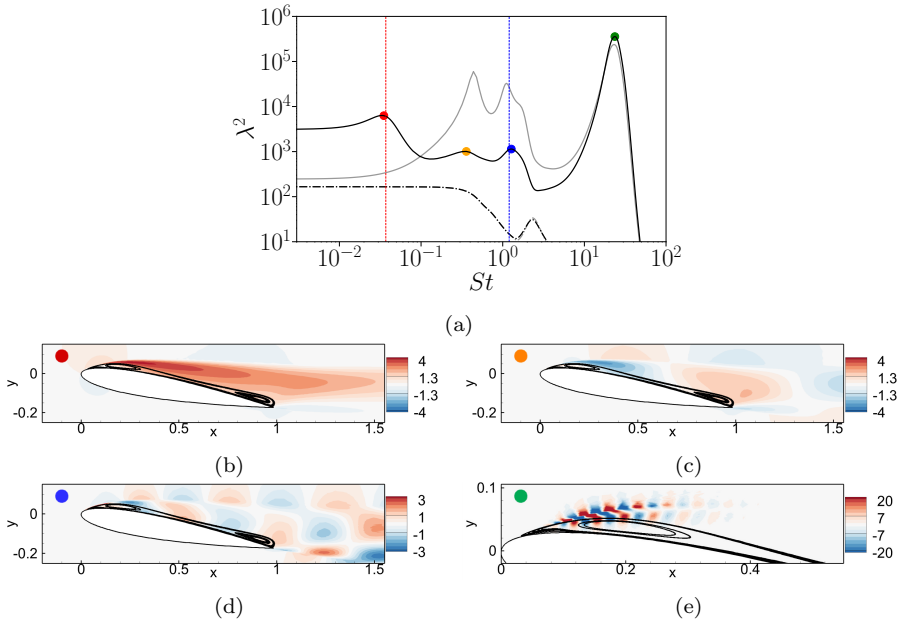

Fig. 13: (a) First (full lines) and second (dash-dotted lines) largest resolvent gains λ^2 at frequency St for the assimilated flow at $Re = 5.4 \cdot 10^4$ in the perturbed (black lines) or frozen (grey lines) eddy-viscosity approach. (b)-(e) Real part of the streamwise velocity component of the dominant resolvent mode in the perturbed approach at (b) low-frequency $St = 0.035$, intermediate frequencies (c) $St = 0.36$ and (d) $St = 1.3$ and high-frequency (e) $St = 24$. The vertical dashed red and blue lines emphasize the low ($St \simeq 0.035$) and intermediate ($St \simeq 1.3$) frequencies, respectively, at which comparisons with the PIV results will be performed.

This range of frequencies is significantly more amplified according to the perturbed eddy-viscosity approach, with a clear distinction between first and second gains, and a peak around $St = 0.035$ which corresponds to the frequency of the above-discussed least stable eigenmode. The spatial structure of the associated dominant resolvent mode, which is shown in figure 13b, is very similar to that of this eigenmode (figure 11d). In the range of intermediate frequencies $0.1 \lesssim St \lesssim 3$, amplification is more pronounced in the frozen eddy-viscosity approach, which suggests that the perturbed eddy-viscosity approach effectively increases diffusion in this range, while two peaks are still identifiable at $St = 0.36$ and $St = 1.3$ in this latter approach. The spatial structure of the corresponding resolvent modes is illustrated in figures 13c and 13d, respectively. The resolvent mode at $St = 1.3$ is related to vortex-shedding phenomena, as the associated non-dimensional frequency that includes the angle of incidence is $St_\alpha = fc\sin(\alpha)/U_b = 0.22$. Finally, in both approaches, the largest amplifications are obtained at higher frequencies ($St > 10$), with a maximum amplification around $St = 24$. As illustrated in figure 13e, this frequency is associated to the development of Kelvin-Helmholtz instabilities in the shear layer of the leading-edge recirculation region. In this region, the base turbulent eddy-viscosity is of the order of the kinematic viscosity, thus

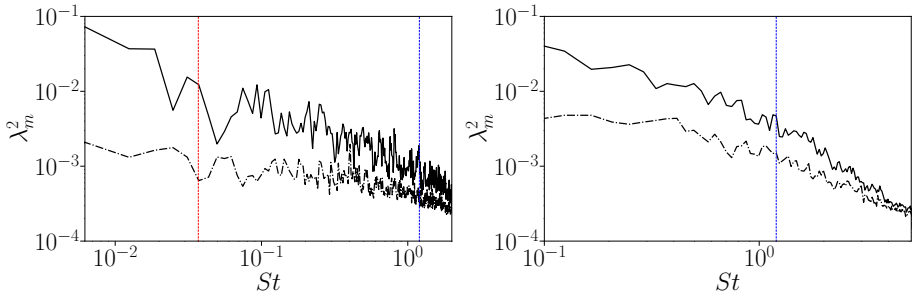

Fig. 14: First (full lines) and second (dash-dotted lines) largest eingenvalues λ_m^2 at frequency St from the SPOD analysis of the PIV measurements at $Re = 5.4 \cdot 10^4$ with (a) 5 and (b) 39 blocks. The vertical dashed red and blue lines emphasize the same low ($St \simeq 0.035$) and intermediate ($St \simeq 1.3$) frequencies, respectively, as in the resolvent analysis results in figure 13a.

explaining the very large amplification of these small-scale structures in a very small region of space. Differences between frozen and perturbed eddy-viscosity approaches appear limited at such high frequencies. Amplification is still slightly larger in the perturbed eddy-viscosity approach.

The outputs of the above resolvent analyses are now compared to the Spectral Proper Orthogonal Decomposition (SPOD) [68] of the PIV measurements. This consists in evaluating a cross-spectral density tensor from the PIV snapshots and computing its eigenvalues and corresponding eigenmodes, which are denoted by λ_m^2 and $\hat{\boldsymbol{u}}_m$, respectively. SPOD modes may be interpreted as coherent fluctuations at a given frequency, and may be equivalent to resolvent modes under certain conditions. Following Welch's method and relying on the implementation in [35], two SPOD are performed, focusing on the characterization of low and intermediate frequencies, respectively. In the first SPOD treatment, the PIV snapshots are divided in 5 blocks with an overlap of 50%, which amounts to 1666 snapshots per block. The minimum frequency that may be captured, which also corresponds to the frequency resolution ΔSt, corresponds to $St_{\min} = \Delta St = 6.2 \cdot 10^{-3}$. This value appears as an upper bound for the identification of the above-discussed low-frequency phenomena. The first and second largest eigenvalues λ_m^2 as functions of frequency for this SPOD treatment are reported in figure 14a. These eigenvalues have been normalized by the global kinetic energy of the measured flow fluctuations. The experimental flow clearly exhibits energetic low-frequency phenomena ($St \lesssim 0.1$) with low-rank dynamics (difference of more than one order of magnitude between first and second eigenvalues). Besides, the SPOD spectrum exhibits a peak at $St \simeq 0.035$ (the exact identified value in the SPOD results, which is constrained by the finite frequency resolution $\Delta St = 6.2 \cdot 10^{-3}$, is $St = 0.037$), as emphasized by the red dashed line. These findings are in close agreement with the resolvent analysis in the perturbed eddy-viscosity approach, while no specific amplification at low-frequencies could be predicted by the frozen one. A peak at the intermediate frequency $St \simeq 1.3$ may also be identified in figure 14a (emphasized by the blue dashed line), as in the resolvent analyses in both perturbed and

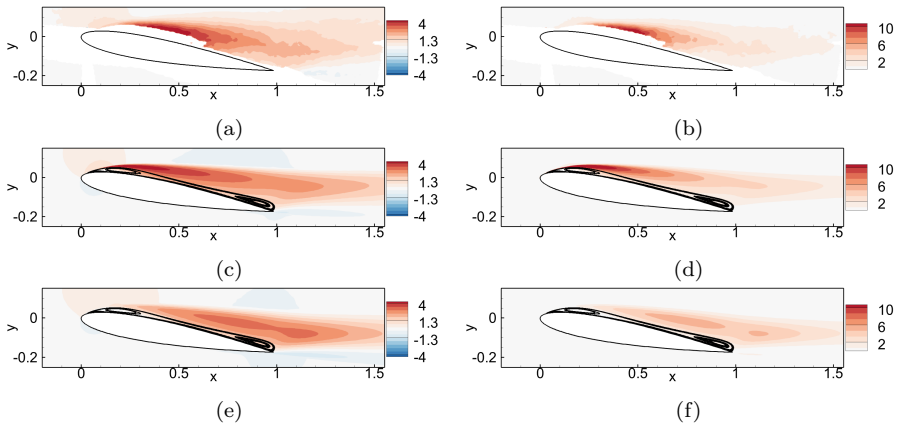

Fig. 15: Real part of the streamwise velocity component (left column) and kinetic energy field (right column) for dominant modes at $St \simeq 0.035$ from the SPOD of the PIV measurements with 5 blocks (top row) and the resolvent analysis around the assimilated flow in the perturbed (middle row) and frozen (bottom row) eddy-viscosity approaches. An animation of the reported modes is provided in Online Resource 1.

St	0.035		1.3	
	perturbed	frozen	perturbed	frozen
M_m	0.141	0.195	0.315	0.320
E_m	0.209	0.338	0.237	0.241

Table 2: Misalignment coefficient M_m and error E_m in (30) between the dominant SPOD mode and resolvent one in the perturbed or frozen eddy-viscosity approach at $St \simeq 0.035$ (see figure 15) and $St \simeq 1.3$ (see figure 16).

frozen approaches. In order to favor a better characterization of intermediate frequencies, a second SPOD treatment is performed based on 39 blocks, still with an overlap of 50%, which corresponds to 250 snapshots per block. In this case, the frequency resolution is $\Delta St = 0.041$. The corresponding eigenvalue spectra are reported in figure 14b, where the peak at $St \simeq 1.3$ persists (the exact identified value in the SPOD results is $St = 1.2$). Beyond increasing the number of blocks in Welch's method, more advanced SPOD approaches, such as based on multitaper estimation [55], could be considered to possibly refine the present results, which is left for future work. It may be noted that, as imposed by the acquisition rate of the PIV measurements (see §3.1), the maximum frequency is $St_{\max} = 5.2$ in the SPOD results. This prevents the latter from identifying the high-frequency Kelvin-Helmholtz fluctuations whose associated frequency is estimated around $St = 24$ through resolvent analysis.

The dominant SPOD modes at the above-discussed low ($St \simeq 0.035$) and intermediate ($St \simeq 1.3$) frequencies are illustrated in figures 15 and 16, respectively, and are compared with the dominant resolvent modes at the same frequencies in the perturbed and frozen eddy-visosity approaches. The left column of these figures reports the real part of the streamwise velocity component for the modes,

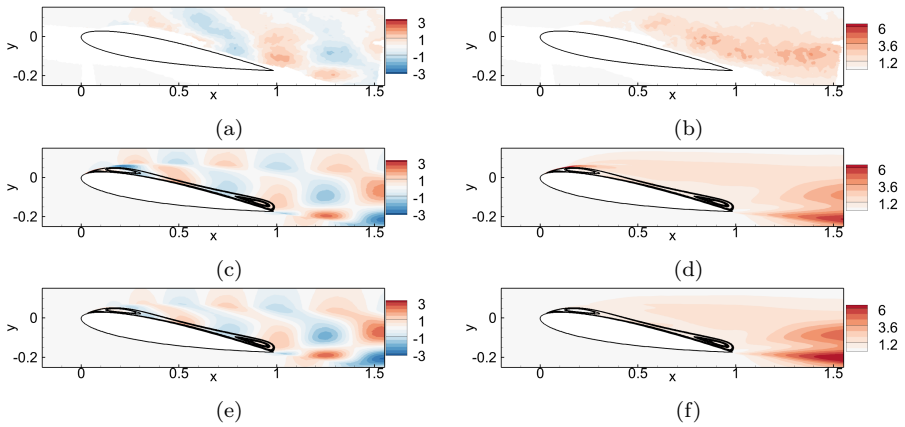

Fig. 16: Real part of the streamwise velocity component (left column) and kinetic energy field (right column) for dominant modes at $St \simeq 1.3$ from the SPOD of the PIV measurements with 39 blocks (top row) and the resolvent analysis around the assimilated flow in the perturbed (middle row) and frozen (bottom row) eddy-viscosity approaches. An animation of the reported modes is provided in Online Resource 2.

noticing that all SPOD and resolvent modes, which are denoted by $\hat{\boldsymbol{u}}_m$ and $\hat{\boldsymbol{u}}$, respectively, have been normalized such that $\|\hat{\boldsymbol{u}}_m\|_{\mathcal{M}} = \|\hat{\boldsymbol{u}}\|_{\mathcal{M}} = 1$, i.e. based on their L^2-norm over the (full) measurement domain. In addition, modes have been multiplied by phase terms according to $e^{\mathrm{i}\varphi_m}\hat{\boldsymbol{u}}_m$ and $e^{\mathrm{i}\varphi}\hat{\boldsymbol{u}}$ such that the reported fields reach their maximum values at $(x, y) = (1, -0.1)$. The right column illustrates the corresponding kinetic energy $\hat{k}_m = \frac{1}{2}\hat{\boldsymbol{u}}_m^{\mathrm{H}}\hat{\boldsymbol{u}}_m$ or $\hat{k} = \frac{1}{2}\hat{\boldsymbol{u}}^{\mathrm{H}}\hat{\boldsymbol{u}}$.

We first consider results at the low frequency $St \simeq 0.035$. In both SPOD results obtained with 5 blocks (figures 15a-15b) and those from the resolvent analysis in the perturbed eddy-viscosity approach (figures 15c-15d), the kinetic energy of the reported mode highly concentrates over the upstream half of the suction side, and in particular over the leading-edge laminar-separation bubble as may be identified from the numerical results. These two modes appear to be in good agreement. On the contrary, the resolvent mode in the frozen-eddy viscosity approach (figures 15e-15f) is more spread over the downstream half of the suction side and beyond, with a vanishing kinetic energy close to the leading edge, and therefore significantly differs from the two above modes. The agreement between SPOD and resolvent modes may be assessed on a more quantitative basis through the two following quantities

$$M_m = 1 - \left|\langle \hat{\boldsymbol{u}}_m, \hat{\boldsymbol{u}} \rangle_{\mathcal{M}}\right|, \quad E_m = \int_{\Omega_m} |\hat{k}_m - \hat{k}|\, d\Omega_m. \tag{30}$$

The first one, M_m, quantifies the misalignment between a SPOD mode $\hat{\boldsymbol{u}}_m$ and a resolvent one $\hat{\boldsymbol{u}}$ in the perturbed or frozen-eddy viscosity approach. The second quantity, E_m, measures the discrepancies in the spatial distribution of kinetic energy of the modes, and forms a possibly more stringent criterion. As modes are normalized such that $\|\hat{\boldsymbol{u}}_m\|_{\mathcal{M}} = \|\hat{\boldsymbol{u}}\|_{\mathcal{M}} = 1$, perfect agreement between SPOD and resolvent modes entails $M_m = E_m = 0$, while maximum deviation corresponds

to $M_m = E_m = 1$, noting that $E_m \leq \int_{\Omega_m} \hat{k}_m \, d\Omega_m + \int_{\Omega_m} \hat{k} \, d\Omega_m = 0.5(\|\hat{\boldsymbol{u}}_m\|^2_{\mathcal{M}} + \|\hat{\boldsymbol{u}}\|^2_{\mathcal{M}}) = 1$. The evaluation of these quantities for the above-discussed dominant modes at $St \simeq 0.035$ is reported in table 2, which confirms the better agreement between SPOD and resolvent analysis in the perturbed eddy-viscosity approach compared to the frozen one in this case. In particular, the error E_m is more than 50% larger in the frozen approach compared to the perturbed one.

We now examine SPOD and resolvent modes at the intermediate frequency $St \simeq 1.3$ in figure 16. At this frequency, resolvent analysis modes in the perturbed (figures 16c-16d) and frozen (figures 16e-16f) eddy-viscosity approaches appear very similar, putting aside a slightly higher kinetic energy above the leading-edge laminar-separation bubble in the perturbed approach compared to the frozen one. Both modes provide a correct estimation of the SPOD mode computed with 39 blocks (figures 16a-16b). These findings may be confirmed through the inspection of table 2. Differences between the SPOD and resolvent modes may still be spotted through figure 16, in particular around the shear layer that originates from the leading edge when comparing the streamwise velocity components (left column), and around the shear layer that originates from the trailing edge when inspecting the kinetic energy fields (right column). Besides, the misalignment coefficient M_m is higher than at low frequency. The value of the error E_m is also higher, although to a lesser extent, compared to that in the perturbed eddy-viscosity approach at low frequency. All these findings suggest that intermediate frequencies are less accurately estimated than lower ones through resolvent analysis (even in the perturbed eddy-viscosity approach) in the present case. Aside from various factors ranging from modelling limitations to difficulties in having access to accurate intermediate- (and high-) frequency content through experiments for explaining these discrepancies, one could wonder whether intermediate frequencies are significantly modulated by the dominant low-frequency oscillations. If so, the quasi-static resolvent and SPOD approaches developed in [18] could be more appropriate to investigate intermediate and higher frequencies, which is left for future studies.

In summary, in the present flow configuration, resolvent analysis based on the perturbed eddy-viscosity approach provides a significantly more accurate insight into low-frequency oscillations compared to the frozen approach. First, it allows to identify a peak of amplification at a low frequency that is close to that observed in the PIV data, while no particular amplification is predicted in the frozen approach. In addition, the resolvent mode that is predicted in the perturbed eddy-viscosity approach is in good agreement with the experimental SPOD mode at the corresponding frequency, which is not the case in the frozen approach. On the other hand, at intermediate frequencies, while relying or not on the perturbed approach still has an impact on the value of the resolvent gains, the shape of the associated modes appears relatively unaffected by this modelling choice.

4.4 Variation in Reynolds number

The present combination of PIV-data assimilation for improving a RANS-based mean-flow estimation followed by resolvent analysis around the latter is further applied at other Reynolds numbers in the range $4.3 \cdot 10^4 \leq Re \leq 6.4 \cdot 10^4$. The results of the data assimilation step (based on the full PIV mean-velocity fields) are first illustrated in figure 17, which reports the streamwise velocity of the assimilated

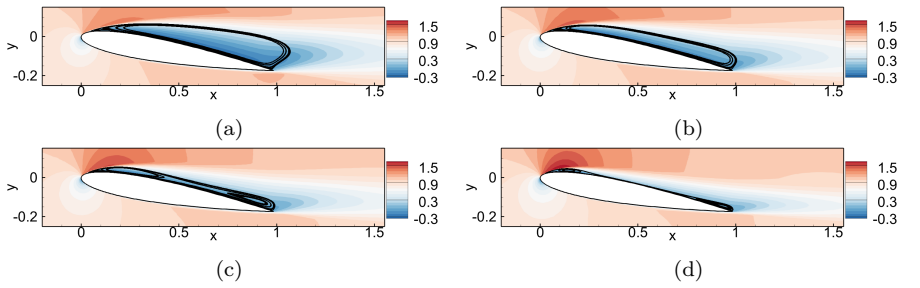

Fig. 17: Mean streamwise velocity for assimilated RANS solution at (a) $Re = 4.3 \cdot 10^4$, (b) $Re = 5.1 \cdot 10^4$, (c) $Re = 5.3 \cdot 10^4$ and (d) $Re = 6.4 \cdot 10^4$, respectively.

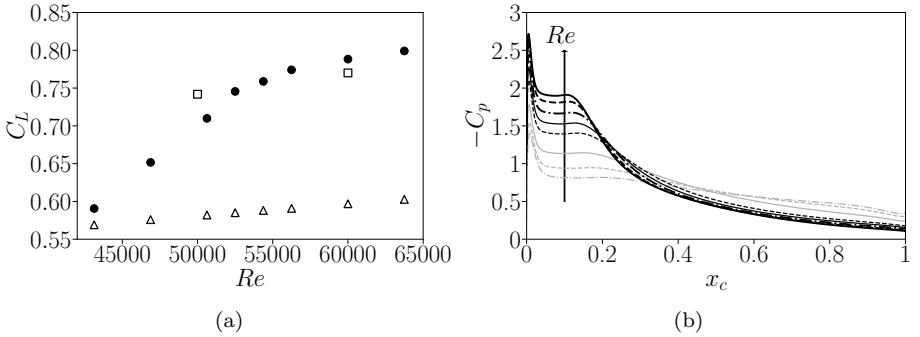

Fig. 18: (a) Lift coefficient for baseline (open triangles) and assimilated (full circles) RANS. Experimental results from [43] are also reported (empty squares). (b) Pressure coefficient at the suction side for assimilated RANS at $4.3{\cdot}10^4 \leq Re \leq 6.4{\cdot}10^4$.

mean flow for some representative cases. For $Re < 5 \cdot 10^4$, the mean flow is massively separated on the suction side of the airfoil with a large recirculation region extending from the leading-edge to the trailing-edge, as illustrated in figure 17a. When increasing the Reynolds number, the size of the recirculation region progressively shrinks while two connected leading-edge and trailing-edge recirculation regions appear (figure 17c), similarly as in the above-discussed case $Re = 5.4 \cdot 10^4$. For the largest Reynolds number that is investigated here ($Re = 6.4 \cdot 10^4$, figure 17d), the flow is close to fully reattach after the leading-edge laminar-separation bubble and thus corresponds to almost pre-stall conditions.

The reconstructed lift coefficient and pressure distribution over the suction side for all available cases are illustrated through figure 18. We should recall that none of these quantities would have been accessible without data assimilation since the present experimental campaign was restricted to PIV measurements. Figure 18a confirms the significant alteration of the lift coefficient through the data-assimilation procedure between the baseline solution (open triangles) and the assimilated one (full circles), in particular for $Re \geq 5 \cdot 10^4$. The lift coefficient of the baseline RANS solution barely changes with the Reynolds number. Its low value $C_L \sim 0.6$ corresponds to that of a fully detached solution (see figure 3a). The baseline model is thus not able to capture the flow reattachment that comes along

with an increase of the lift, as observed for the assimilated solution. For the sake of validation, experimental results that were obtained in [43] for the same flow configuration as the present one (NACA0012 airfoil at an incidence of 10°) are also shown in figure 18a with square symbols. They favorably compare to the lift coefficient of the assimilated RANS solutions, confirming the quality of the latter. Figure 18b allows to assess the development of a plateau in the C_p distribution in the assimilated RANS results for increasing Reynolds number which is linked to the appearance of the laminar-separation bubble close to the leading edge.

Resolvent analysis in the perturbed eddy-viscosity approach is then performed around the various assimilated flows. The dominant resolvent gain is reported in figure 19a as a function of the non-dimensional frequency for all investigated values of Re. As already evidenced for $Re = 5.4 \cdot 10^4$ (figure 13), different peaks may be identified at low, intermediate and high frequency. The associated frequencies are denoted as St_L, St_I and St_H, respectively, and are associated with the red, blue and green colors, respectively, throughout figure 19. They are emphasized through vertical dotted and dashed lines in figure 19a for the lowest ($Re = 4.3 \cdot 10^4$) and highest ($Re = 6.4 \cdot 10^4$) investigated values of Re, respectively. The evolution of these frequencies with respect to Re is further illustrated through figures 19b-19d, while the values of the corresponding gains is reported in figure 19e. This latter figure may help in distinguishing between two regimes in the present results. Below a threshold value that is approximated as $Re \simeq 5.2 \cdot 10^4$ (and emphasized through dashed vertical lines in figures 19b-19e), the low-frequency peak is actually not-well pronounced, and both intermediate and high frequencies are more amplified. On the contrary, above this threshold, the low-frequency peak becomes well pronounced and dominates over intermediate frequencies. This qualitative change seems to coincide with the formation of two connected leading-edge and trailing-edge recirculation regions, as previously discussed based on figure 17.

Finally, we examine in more detail the characteristics of the frequency peaks. Above the threshold $Re \simeq 5.2 \cdot 10^4$, the low frequency St_L appears weakly sensitive with respect to Re in the investigated range (figure 19b). It may be noted in figure 19e that the value of the corresponding gain, after an increase in Re from $Re \simeq 5.2 \cdot 10^4$, seems to saturate and even slightly decrease after $Re \simeq 6 \cdot 10^4$. Data at higher Re would be required to confirm this trend. Concerning the intermediate-frequency peak, the associated gain monotonically decreases over the full range of investigated Re values (figure 19e). St_I increases sightly with Re, with a relatively abrupt change around $Re \simeq 6 \cdot 10^4$ (figure 19c). Above this latter Re value, the peak at St_I, which should correspond to vortex-shedding phenomena, actually becomes less pronounced than another intermediate peak around $St \simeq 0.36$ (already identified in figure 13), as may be inferred from figure 19a. High-frequencies that are related to the development of Kelvin-Helmholtz instabilities remain the most amplified frequencies at all Re (figure 19e). The associated frequency St_H monotonically and significantly increases with Re (figure 19d). Such an evolution is likely related to the decrease in the characteristic length scale that is associated to this frequency, namely the shear layer thickness at the leading edge.

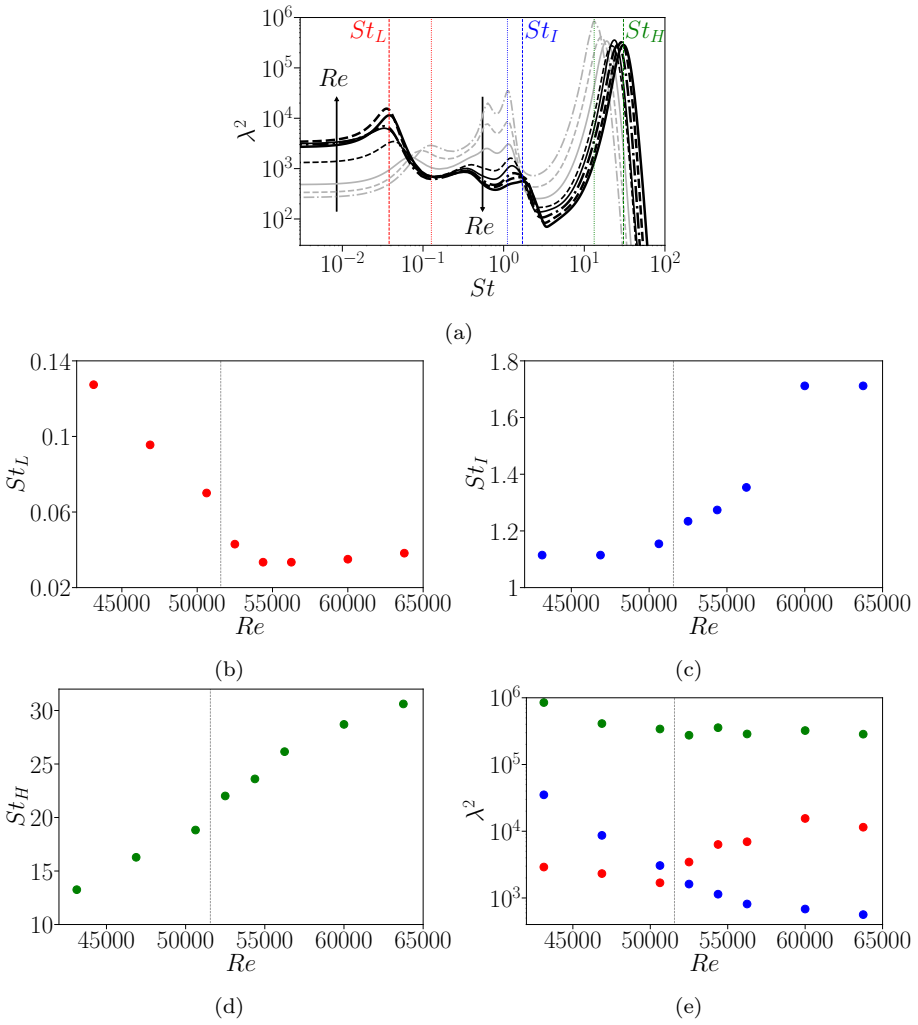

Fig. 19: (a) Largest resolvent gain λ^2 in the perturbed eddy-viscosity approach at frequency St for assimilated flows at various Reynolds numbers. Grey lines correspond to $4.3 \cdot 10^4 \leq Re \leq 5.1 \cdot 10^4$, while black ones correspond to $5.3 \cdot 10^4 \leq Re \leq 6.4 \cdot 10^4$. Vertical dotted and dashed lines emphasize, for $Re = 4.3 \cdot 10^4$ and $Re = 6.4 \cdot 10^4$ respectively, the frequencies St_L (red lines), St_I (blue lines) and St_H (green lines) that correspond to peaks of amplification at low, intermediate and high frequency, respectively. (b-d) Evolution of (b) St_L, (c) St_I and (d) St_H with Re. (e) Values of the gains that are reached at these frequencies. In (b-e), red, blue and green circles correspond to the frequencies St_L, St_I and St_H, respectively, while the vertical dashed lines indicate the approximate Reynolds number $Re \simeq 5.2 \cdot 10^4$ above which the low-frequency peak at St_L is clearly identified and dominant compared to that at St_I. Grey and black lines in (a) thus correspond to values of Re that are below and above this threshold, respectively.

5 Conclusions

The near-stall flow past a NACA0012 airfoil has been investigated through a combination of data assimilation and linear mean-flow analyses in a two-step procedure. Time-averaged PIV measurements have first been assimilated into RANS simulations based on the Spalart-Allmaras model through the optimization of a corrective field in the latter. Data assimilation has allowed to considerably improve the baseline RANS prediction and to reconstruct the flow in regions that were not accessible in the PIV data. This could be achieved even when relying on data in a small subdomain. The so-obtained mean-flows and corrected RANS equations have then been employed in linear mean-flow analyses. Global stability analysis has already allowed to identify near-stall low-frequency modes. This could be achieved when taking into account perturbations in the turbulent eddy-viscosity through the linearized corrected Spalart-Allmaras model, but not in a frozen approach. Resolvent analysis has then been performed, comparing with the SPOD of the PIV snapshots. Besides of vortex-shedding and Kelvin-Helmholtz phenomena, resolvent analysis in the perturbed eddy-viscosity approach has also identified the amplification of low frequencies in accordance with the SPOD results, contrary to the frozen approach. In addition, the dominant low-frequency resolvent mode in the perturbed approach has been shown to be close to its SPOD counterpart, while the mode in the frozen approach exhibited significant discrepancies. Differences between the perturbed and frozen approaches have appeared to lessen at higher frequencies, in particular concerning the mode shapes.

In summary, the present study illustrates the potentialities in relying on data assimilation, RANS modelling and linear analyses for the prediction of coherent fluctuations in turbulent flows that involve a wide range of dynamic scales from limited mean-flow measurements. While turbulence modelling and the use of the perturbed eddy-viscosity approach have been shown to play a determinant role in the correct estimation of near-stall low-frequency phenomena in the present flow configuration, the possible generalisation of such findings remains to be done. Incidentally, a recent study [14] suggests that a frozen-eddy viscosity approach is sufficient to estimate the low-frequency dynamics of a pressure-gradient-induced turbulent separation bubble. Accordingly, the determination of the conditions under which a perturbed eddy-viscosity approach is actually necessary for the correct prediction of coherent fluctuations could be the subject of future work. A related open question that is worth further investigation concerns the influence of the choice of the turbulence model in the perturbed approach.

Acknowledgements The authors are grateful to B. Leclaire, first as coordinator of two research projects in which this study was carried out, and for providing useful suggestions about the manuscript. The authors acknowledge many valuable discussions with F. Champagnat about this study, in particular concerning modal analyses and results interpretation. A. Gounand, C. Illoul, J.-C. Monnier, R. Soares Morgadinho and J. Pruvost are thanked for their involvement in the experimental campaign that provided the present measurements. Y. Le Sant is also thanked for the development of specific post-processing tools for the particle images. Finally, the authors are grateful to F. Nicolas for his precious help on using these latter tools and for providing first PIV fields.

Declarations

Conflict of interest

The authors declare that they have no conflict of interest.

Ethical Approval

Compliance with ethical standards.

Funding

This study benefited from no specific funding.

Availability of data and materials

All data that support the findings of this study are included within the article.

Appendix A Details on the employed Spalart-Allmaras model

We here provide the exact version of the Spalart-Allmaras model [59] that is employed in the present study. The governing equation for the pseudo-eddy viscosity variable $\langle\tilde{\nu}\rangle$ is given in (4). From $\langle\tilde{\nu}\rangle$, the actual turbulent eddy-viscosity that is involved in the momentum equations is obtained from

$$\nu_t(\langle\tilde{\nu}\rangle) = \langle\tilde{\nu}\rangle\, f_{v1}, \quad f_{v1} = \frac{\chi^3}{\chi^3 + c_{v1}^3}, \quad \chi = \langle\tilde{\nu}\rangle\, Re, \quad c_{v1} = 7.1. \tag{31}$$

The diffusion coefficient $\eta(\langle\tilde{\nu}\rangle)$ in (4) is evaluated in a negative continuation form [41] according to

$$\eta = \begin{cases} \frac{1}{Re\,\sigma}(1+\chi) & \chi \geq 0 \\ \frac{1}{Re\,\sigma}(1+\chi+0.5\chi^2) & \chi < 0 \end{cases}, \quad \sigma = \frac{2}{3}. \tag{32}$$

The source term $s(\langle\boldsymbol{u}\rangle, \langle\tilde{\nu}\rangle) = P_{\tilde{\nu}} + D_{\tilde{\nu}} + C_{\tilde{\nu}}$ in (4) includes production, destruction and cross-diffusion terms. The production one is evaluated as

$$P_{\tilde{\nu}} = \begin{cases} \gamma_{BC} c_{b1} \tilde{\Omega}\, \langle\tilde{\nu}\rangle & \chi \geq 0 \\ \gamma_{BC} c_{b1} \Omega_u\, \langle\tilde{\nu}\rangle\, g_n & \chi < 0 \end{cases}, \tag{33}$$

with

$$\tilde{\Omega} = \Omega_u + \frac{f_{v2}\,\langle\tilde{\nu}\rangle}{\kappa^2 d^2},\ \Omega_u = \|\nabla \times \langle\boldsymbol{u}\rangle\|,\ f_{v2} = 1 - \frac{\chi}{1+\chi f_{v1}},\ g_n = 1 - \frac{1000\chi^2}{1+\chi^2}, \tag{34}$$

where d corresponds to the distance to the walls, $\|\circ\|$ here refers to the (local) Euclidean norm, while $c_{b1} = 0.1355$ and $\kappa = 0.41$. The production term here includes the transition model proposed in [41] which is given by

$$\gamma_{BC} = 1 - \exp(-\sqrt{\tau_1} - \sqrt{\tau_2}),\ \tau_1 = \frac{\max(Re_\theta - Re_{\theta c}, 0)}{\chi_1 Re_{\theta c}},\ \tau_2 = \max\left(\frac{Re\,\nu_t}{\chi_2}, 0\right), \tag{35}$$

with

$$Re_\theta = \frac{\Omega_u d^2 Re}{2.193}, \quad Re_{\theta c} = 803.73(Tu_\infty + 0.6067)^{-1.027}, \tag{36}$$

and where we use $Tu_\infty = 0.01$, $\chi_1 = 0.002$ and $\chi_2 = 0.02$. The cross-diffusion and destruction terms are evaluated according to

$$C_{\tilde{\nu}} = \frac{c_{b2}}{\sigma}\|\nabla\langle\tilde{\nu}\rangle\|, \quad D_{\tilde{\nu}} = \begin{cases} -c_{w1} f_w \frac{\langle\tilde{\nu}\rangle^2}{d^2} & \chi \geq 0 \\ c_{w1}\frac{\langle\tilde{\nu}\rangle^2}{d^2} & \chi < 0 \end{cases}, \tag{37}$$

with

$$f_w = g\left(\frac{1 + c_{w3}^6}{g^6 + c_{w3}^6}\right)^{\frac{1}{6}},\ g = r + c_{w2LRe}(r^6 - r),\ c_{w2LRe} = c_{w4} + \frac{c_{w5}}{(1 + \frac{\chi}{40})^2}, \tag{38}$$

and

$$r = \begin{cases} 10 & r' < 0, r' > 10 \\ r' & 0 \leq r' \leq 10 \end{cases}, \quad r' = \frac{\langle\tilde{\nu}\rangle}{\tilde{\Omega} d^2 \kappa^2}. \tag{39}$$

It may be emphasized that the low-Reynolds expression c_{w2LRe} proposed in [60] is here employed (instead of $c_{w2LRe} = c_{w2}$ being a constant). Constants are given by $c_{b2} = 0.622$, $c_{w1} = \frac{c_{b1}}{\kappa^2} + \frac{1+c_{b2}}{\sigma}$, $c_{w3} = 2$, $c_{w4} = 0.21$ and $c_{w5} = 1.5$.

Appendix B On the choice of the turbulence-modelling correction

In this appendix, we discuss the present choice of turbulence-modelling correction with respect to previous proposals in the literature. It may be first mentioned that corrections in the momentum equations such as proposed in [17] have been ruled out in the present study to preserve the full modelling of the Reynolds stress tensor for turbulent fluctuations. We therefore only compare corrections to the Spalart-Allmaras equation (4) in this appendix. Figure 20 first reports the turbulent eddy-viscosity field for the baseline RANS solution at $Re = 5.4 \cdot 10^4$ (figure 20a), along with the field $|\hat{\tilde{\nu}}^\dagger||\hat{\boldsymbol{q}}|$ (figure 20b), with $|\hat{\boldsymbol{q}}| = (\hat{\boldsymbol{q}}^{\mathrm{H}}\hat{\boldsymbol{q}})^{\frac{1}{2}}$, where $\hat{\boldsymbol{q}}$ and $\hat{\tilde{\nu}}^\dagger$ refer to the least stable (low-frequency) mode and to the eddy-viscosity component of the associated adjoint mode (see (28)), still for the baseline RANS solution. The field $|\hat{\tilde{\nu}}^\dagger||\hat{\boldsymbol{q}}|$ provides an upper bound for the variation in the associated eigenvalue $|\delta\mu|$ that is induced by a local and unitary change in the Spalart-Allmaras equation [19]. As mentioned in §2.2.2, a turbulence-modelling correction $f_{\tilde{\nu}}$ is here considered as appropriate if it acts in turbulent regions, thus has a strong overlap with ν_t, and, on the contrary, vanishes in regions with high structural sensitivity, namely that correspond to high values for the sensitivity field $|\hat{\tilde{\nu}}^\dagger||\hat{\boldsymbol{q}}|$. Compliance with this latter criterion prevents small variations in $f_{\tilde{\nu}}$ from having a large impact on the

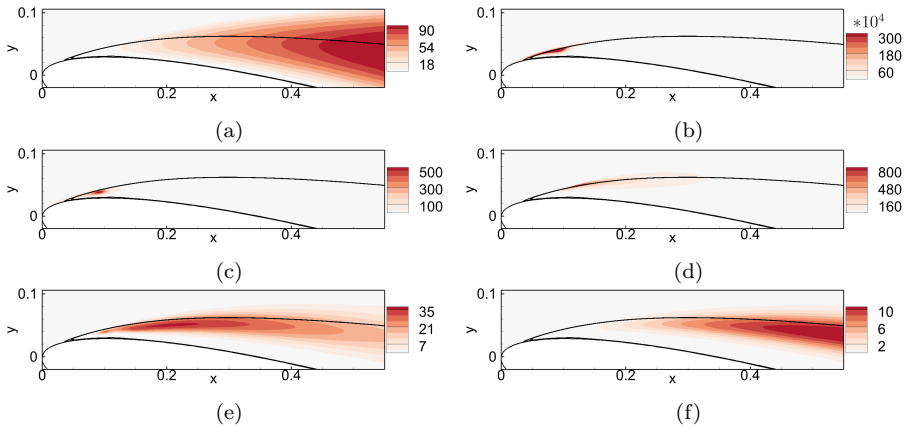

Fig. 20: (a) Turbulent eddy-viscosity field ν_t for the baseline RANS solution at $Re = 5.4 \cdot 10^4$ and (b) sensitivity field $|\hat{\tilde{\nu}}^\dagger||\hat{\boldsymbol{q}}|$ for the least stable mode. (c-f) Update of the turbulence-modelling correction $f_{\tilde{\nu}}$ when (c) $f_{\tilde{\nu}} = g$, (d) $f_{\tilde{\nu}} = gP_{\tilde{\nu}}$, (e) $f_{\tilde{\nu}} = g\bar{\tilde{\nu}}$ and (f) $f_{\tilde{\nu}} = g\bar{\tilde{\nu}}^2$ (present choice).

stability results and facilitate the convergence in the latter. In the rest of figure 20, the identified correction $f_{\tilde{\nu}}$ at the first iteration of the data assimilation procedure (corresponding to a steepest descent update to the baseline case $f_{\tilde{\nu}} = 0$) is reported for various choices of the functional form for this correction. In all cases, g refers to the spatially-dependent control vector in the data assimilation procedure. The direct optimization of $f_{\tilde{\nu}}$ ($f_{\tilde{\nu}} = g$) [17] leads to a correction with a strong overlap with the sensitivity field (figure 20c). The same applies, albeit to a slightly lesser extent, when adjusting a multiplicative field in front of the production term, i.e. when $f_{\tilde{\nu}} = gP_{\tilde{\nu}}$ [57] (figure 20d). The consideration of the functional form $f_{\tilde{\nu}} = g\bar{\tilde{\nu}}$ [11] allows to concentrate the correction in more turbulent regions compared to previous cases, but still does not prevent from significant contributions in the sensitive region (figure 20e). On the contrary, the present proposal $f_{\tilde{\nu}} = g\bar{\tilde{\nu}}^2$ (figure 20f) has a negligible overlap with the sensitivity field and further concentrates in regions that are associated to high values of ν_t, which justifies its use in this study. It may be emphasized that the present choice remains empirical, and is certainly not unique. Incidentally, other expressions involving higher powers of $\bar{\tilde{\nu}}$ (e.g. $f_{\tilde{\nu}} = g\bar{\tilde{\nu}}^3$) were investigated. It appeared in these cases that the correction $f_{\tilde{\nu}}$ was too much constrained downstream of the leading edge, preventing the data-assimilation procedure to satisfactorily reconstruct the mean flow. Future work could be dedicated to the development of a more systematic approach to identify appropriate functional forms for the modelling correction.

References

1. AlMutairi, J., ElJack, E., AlQadi, I.: Dynamics of laminar separation bubble over NACA-0012 airfoil near stall conditions. The Aeronautical Journal **68**, 193–203 (2017)
2. Baker, S., Matthews, I.: Lucas-Kanade 20 Years On: A Unifying Framework. International Journal of Computer Vision **56**, 221–255 (2004)

3. Balay, S., Gropp, W.D., Curfman McInnes, L., Smith, B.F.: Efficient management of parallelism in object oriented numerical software libraries. In: E. Arge, A.M. Bruaset, H.P. Langtangen (eds.) Modern Software Tools in Scientific Computing, pp. 163–202. Birkhäuser Press (1997)
4. Barkley, D.: Linear analysis of the cylinder wake mean flow. Europhysics Letters **75**(5), 750 (2006)
5. Ben Ali, M.Y., Tissot, G., Aguinaga, S., Heitz, D., Mémin, E.: Mean wind flow reconstruction of a high-rise building based on variational data assimilation using sparse pressure measurements. Journal of Wind Engineering and Industrial Aerodynamics **231**, 105,204 (2022)
6. Beneddine, S., Sipp, D., Arnault, A., Dandois, J., Lesshafft, L.: Conditions for validity of mean flow stability analysis. Journal of Fluid Mechanics **798**, 485–504 (2016)
7. Bernardos, L., Richez, F., Gleize, V., Gerolymos, G.A.: Algebraic Nonlocal Transition Modeling of Laminar Separation Bubbles Using $k-\omega$ Turbulence Models. AIAA Journal **57**, 553–565 (2019)
8. Broeren, A.P., Bragg, M.B.: Flowfield Measurements over an Airfoil During Natural Low-Frequency Oscillations near Stall. AIAA Journal **130-132**, 425–433 (1999)
9. Brooks, A.N., Hughes, T.J.R.: Streamline upwind/Petrov-Galerkin formulations for convection dominated flows with particular emphasis on the incompressible Navier-Stokes equations. Computer Methods in Applied Mechanics and Engineering **32**, 199–259 (1982)
10. Busquet, D., Marquet, O., Richez, F., Juniper, M., Sipp, D.: Bifurcation scenario for a two-dimensional static airfoil exhibiting trailing edge stall. Journal of Fluid Mechanics **928**, A3 (2021)
11. Cato, A.S., Volpiani, P.S., Mons, V., Marquet, O., Sipp, D.: Comparison of different data-assimilation approaches to augment RANS turbulence models. Computers & Fluids **266**, 106,054 (2023)
12. Champagnat, F., Plyer, A., Le Besnerais, G., Leclaire, B., Davoust, S., Le Sant, Y.: Fast and accurate PIV computation using highly parallel iterative correlation maximization. Experiments in Fluids **50**, 1169–1182 (2011)
13. Crouch, J.D., Garbaruk, A., Magidov, D.: Predicting the onset of flow unsteadiness based on global instability. Journal of Computational Physics **224**, 924–940 (2007)
14. Cura, C., Hanifi, A., Cavalieri, A.V.G., Weiss, J.: On the Low-Frequency Dynamics of Turbulent Separation Bubbles p. arXiv:2311.13446 (2023)
15. Eljack, E., Soria, J., Elawad, Y., Ohtake, T.: Simulation and characterization of the laminar separation bubble over a NACA-0012 airfoil as a function of angle of attack. Physical Review Fluids **6**, 034,701 (2021)
16. Foures, D.P.G., Dovetta, N., Sipp, D., Schmid, P.J.: A data-assimilation method for Reynolds-averaged Navier-Stokes-driven mean flow reconstruction. Journal of Fluid Mechanics **759**, 404–431 (2014)
17. Franceschini, L., Sipp, D., Marquet, O.: Mean-flow Data Assimilation based on minimal correction of turbulence models: Application to turbulent high-Reynolds number backward-facing step. Physical Review Fluids **5**, 094,603 (2020)
18. Franceschini, L., Sipp, D., Marquet, O., Moulin, J., Dandois, J.: Identification and reconstruction of high-frequency fluctuations evolving on a low-frequency periodic limit cycle: application to turbulent cylinder flow. Journal of Fluid Mechanics **942**, A28 (2022)
19. Giannetti, F., Luchini, P.: Structural sensitivity of the first instability of the cylinder wake. Journal of Fluid Mechanics **581**, 167–197 (2007)
20. Hansen, P.C., O'Leary, D.P.: The use of the L-curve in the regularization of discrete ill-posed problems. SIAM Journal on Scientific Computing **14**, 1487–1503 (1993)
21. Hayase, T.: Numerical simulation of real-world flows. Fluid Dynamics Research **47**, 051,201 (2015)
22. Hecht, F.: New development in FreeFem++. Journal of Numerical Mathematics **20**, 251–265 (2012)
23. Hussain, A.K.M.F., Reynolds, M.C.: The mechanics of an organized wave in turbulent shear flow. Journal of Fluid Mechanics **41**, 241–258 (1970)
24. Iorio, M.C., Gonzalez, L.M., Martínez-Cava, A.: Global stability analysis of a compressible turbulent flow around a high-lift configuration. AIAA Journal **54**, 373–385 (2016)
25. Kuhn, P., Müller, J.S., Knechtel, S., Soria, J., Oberleithner, K.: Influence of Eddy Viscosity on Linear Modeling of Self-Similar Coherent Structures in the Jet Far Field pp. AIAA SciTech Forum 2022–0460 (2022)

26. Le Dimet, F.X., Talagrand, O.: Variational algorithms for analysis and assimilation of meteorological observations: theoretical aspects. Tellus A **38A**, 97–110 (1986)
27. Lehoucq, R.B., Sorensen, D.C., Yang, C.: ARPACK users' guide: solution of large-scale eigenvalue problems with implicitly restarted Arnoldi methods. SIAM (1998)
28. Lewis, J.M., Lakshmivarahan, S., Dhall, S.K.: Dynamic data assimilation: a least squares approach, *Encyclopedia of Mathematics and its Applications*, vol. 104. Cambridge University Press (2006)
29. Marquet, O., Leontini, J.S., Zhao, J., Thompson, M.C.: Hysteresis of two-dimensional flows around a NACA0012 airfoil at Re = 5000 and linear analyses of their mean flow. International Journal of Heat and Fluid Flow **94**, 108,920 (2022)
30. Marquet, O., Lesshafft, L.: Identifying the active flow regions that drive linear and nonlinear instabilities p. arXiv:1508.07620 (2015)
31. McCullough, G.B., Gault, D.E.: Examples of three representative types of airfoil section stall at low speed p. NASA Technical Note 2502 (1951)
32. McKeon, B.J., Sharma, A.S.: A critical-layer framework for turbulent pipe flow. Journal of Fluid Mechanics **658**, 336–382 (2010)
33. Meliga, P., Pujals, G., Serre, E.: Sensitivity of 2-D turbulent flow past a D-shaped cylinder using global stability. Physics of Fluids **24**, 061,701 (2012)
34. Mendez, M.A., Raiola, M., Masullo, A., Discetti, S., Ianiro, A., Theunissen, R., Buchlin, J.M.: POD-based background removal for particle image velocimetry. Experimental Thermal and Fluid Science **80**, 181–192 (2017)
35. Mengaldo, G., Maulik, R.: PySPOD: A Python package for Spectral Proper Orthogonal Decomposition (SPOD). Journal of Open Source Software **6**, 2862 (2021)
36. Moise, P., Zauner, M., Sandham, N.D.: Connecting transonic buffet with incompressible low-frequency oscillations on aerofoils. Journal of Fluid Mechanics **981**, A23 (2024)
37. Mons, V., Marquet, O.: Linear and nonlinear sensor placement strategies for mean-flow reconstruction via data assimilation. Journal of Fluid Mechanics **923**, A1 (2021)
38. Mons, V., Marquet, O., Leclaire, B., Cornic, P., Champagnat, F.: Dense velocity, pressure and Eulerian acceleration fields from single-instant scattered velocities through Navier–Stokes-based data assimilation. Measurement Science and Technology **33**, 124,004 (2022)
39. Morra, P., Semeraro, O., Henningson, D., Cossu, C.: On the relevance of Reynolds stresses in resolvent analyses of turbulent wall-bounded flows. Journal of Fluid Mechanics **867**, 969–984 (2019)
40. Moulin, J., Jolivet, P., Marquet, O.: Augmented Lagrangian preconditioner for large-scale hydrodynamic stability analysis. Computer Methods in Applied Mechanics and Engineering **351**, 718–743 (2019)
41. Mura, R., Cakmakcioglu, S.C.: A Revised One-Equation Transitional Model for External Aerodynamics - Part I: Theory, Validation and Base Cases p. 2714 (2020)
42. Nocedal, J.: Updating Quasi-Newton Matrices With Limited Storage. Mathematics of Computation **35**, 773–782 (1980)
43. Ohtake, T., Nakae, Y., Motohashi, T.: Nonlinearity of the Aerodynamic Characteristics of NACA0012 Aerofoil at Low Reynolds Numbers. Japan Society of Aeronautical Space Sciences **55**, 439–445 (2007)
44. Olshanskii, M., Lube, G., Heister, T., Löwe, J.: Grad–div stabilization and subgrid pressure models for the incompressible Navier–Stokes equations. Computer Methods in Applied Mechanics and Engineering **198**, 3975–3988 (2009)
45. Paladini, E., Marquet, O., Sipp, D., Robinet, J.C., Dandois, J.: Various approaches to determine active regions in an unstable global mode: application to transonic buffet. Journal of Fluid Mechanics **881**, 617–647 (2019)
46. Peter, J.E.V., Dwight, R.P.: Numerical sensitivity analysis for aerodynamic optimization: A survey of approaches. Computers & Fluids **39**, 373–391 (2010)
47. Pickering, E., Rigas, G., Schmidt, O.T., Sipp, D., Colonius, T.: Optimal eddy viscosity for resolvent-based models of coherent structures in turbulent jets. Journal of Fluid Mechanics **917**, A29 (2021)
48. Raffel, M., Willert, C.E., Scarano, F., Kähler, C.J., Wereley, S.T., Kompenhans, J.: Particle image velocimetry: a practical guide. Springer (2018)
49. Rinoie, K., Takemura, N.: Oscillating behaviour of laminar separation bubble formed on an aerofoil near stall. The Aeronautical Journal **108**, 153–163 (2004)
50. Rodríguez, I., Lehmkuhl, O., Borrell, R., Oliva, A.: Direct numerical simulation of a NACA0012 in full stall. International Journal of Heat and Fluid Flow **43**, 194–203 (2013)

51. Sagaut, P.: Large-eddy simulation for incompressible flows. An introduction, third edition. Springer-Verlag (2005)
52. von Saldern, J.G.R., Reumschüssel, J.M., Kaiser, T.L., Schmidt, O.T., Jordan, P., Oberleithner, K.: Self-consistent closure modeling for linearized mean field methods pp. AIAA AVIATION Forum 2023–4351 (2023)
53. Sandham, N.D.: Transitional separation bubbles and unsteady aspects of aerofoil stall. The Aeronautical Journal **112**, 395–404 (2008)
54. Sartor, F., Mettot, C., Sipp, D.: Stability, Receptivity, and Sensitivity Analyses of Buffeting Transonic Flow over a Profile. AIAA Journal **53**, 1980–1993 (2015)
55. Schmidt, O.T.: Spectral proper orthogonal decomposition using multitaper estimates. Theoretical and Computational Fluid Dynamics **36**, 741–754 (2022)
56. Schmitz, F.W.: Aerodynamics of the model airplane. part 1 - airfoil measurements p. NASA Technical Memorandum 60976 (1967)
57. Singh, A., Duraisamy, K.: Using field inversion to quantify functional errors in turbulence closures. Physics of Fluids **28**, 045,110 (2016)
58. Sipp, D., Lebedev, A.: Global stability of base and mean flows: a general approach and its applications to cylinder and open cavity flows. Journal of Fluid Mechanics **593**, 333–358 (2007)
59. Spalart, P.R., Allmaras, S.R.: A one-equation turbulence model for aerodynamic flows. La Recherche Aérospatiale **1**, 5–21 (1994)
60. Spalart, P.R., Garbaruk, A.V.: Correction to the Spalart–Allmaras Turbulence Model, Providing More Accurate Skin Friction. AIAA Journal **58**, 1903–1905 (2020)
61. Symon, S., Dovetta, N., McKeon, B.J., Sipp, D., Schmid, P.J.: Data assimilation of mean velocity from 2D PIV measurements of flow over an idealized airfoil. Experiments in Fluids **58**, 61 (2017)
62. Symon, S., Madhusudanan, A., Illingworth, S.J., Marusic, I.: Use of eddy viscosity in resolvent analysis of turbulent channel flow. Physical Review Fluids **8**, 064,601 (2023)
63. Symon, S., Sipp, D., McKeon, B.J.: A tale of two airfoils: resolvent-based modelling of an oscillator versus an amplifier from an experimental mean. Journal of Fluid Mechanics **881**, 51–83 (2019)
64. Tanaka, H.: Flow visualization and PIV measurements of laminar separation bubble oscillating at low frequency on an airfoil near stall. In: 24th International Congress of the Aeronautical Sciences, pp. 1–15 (2004)
65. Tani, I.: Low-speed flows involving bubble separations. Progress in Aerospace Sciences **5**, 70–103 (1964)
66. Thomareis, N., Papadakis, G.: Effect of trailing edge shape on the separated flow characteristics around an airfoil at low reynolds number: A numerical study. Physics of Fluids **29**, 014,101 (2017)
67. Thomareis, N., Papadakis, G.: Resolvent analysis of separated and attached flows around an airfoil at transitional Reynolds number. Physical Review Fluids **3**, 073,901 (2018)
68. Towne, A., Schmidt, O.T., Colonius, T.: Spectral proper orthogonal decomposition and its relationship to dynamic mode decomposition and resolvent analysis. Journal of Fluid Mechanics **847**, 821–867 (2018)
69. Viola, F., Iungo, G.V., Camarri, S., Porté-Agel, F., Gallaire, F.: Prediction of the hub vortex instability in a wind turbine wake: stability analysis with eddy-viscosity models calibrated on wind tunnel data. Journal of Fluid Mechanics **750**, R1 (2014)
70. Winkelmann, A.E., Barlow, J.B.: Flowfield Model for a Rectangular Planform Wing beyond Stall. AIAA Journal **18**, 425–433 (1980)
71. Yeh, C.A., Benton, S.I., Taira, K., Garmann, D.J.: Resolvent analysis of an airfoil laminar separation bubble at re= 500 000. Physical Review Fluids **5**, 083,906 (2020)
72. Yeh, C.A., Taira, K.: Resolvent-analysis-based design of airfoil separation control. Journal of Fluid Mechanics **867**, 572–610 (2019)
73. Zaman, K.B.M.Q., McKinzie, D.J., Rumsey, C.L.: A natural low-frequency oscillation of the flow over an airfoil near stalling conditions. Journal of Fluid Mechanics **202**, 403–442 (1989)